

Characterization of optical losses using microdisk cavities

by

A.G.J. Harms

to obtain the degree of Master of Science
at the Delft University of Technology,
to be defended publicly on Monday November 20, 2017 at 2:00 PM.

Student number:	4158679	
Project duration:	August 17, 2016 – November 20, 2017	
Thesis committee:	Dr. S. Gröblacher,	TU Delft, supervisor
	Dr. S. F. Pereira,	TU Delft
	Prof. Dr. Y. M. Blanter,	TU Delft

An electronic version of this thesis is available at <http://repository.tudelft.nl/>.

Abstract

Optical losses due to microfabrication processes have a limiting effect on the progress of research in nanophotonics and optomechanics. Three measurement methods using microdisk cavities have been implemented and tested to characterize these fabrication processes. As published by Borselli et al. (*Optics Express*, 13(5), 2005), the radius dependence of the loss terms can be used to separate surface scattering and surface absorption losses from bulk absorption losses by measuring multiple microdisks with increasing radii. For this radius-varying measurement method the theory was extended in order to use transverse electric resonant modes for measurements. A qualitative difference in surface roughness between two sets of silicon microdisks fabricated with a different electron-beam lithography dosing pattern was able to be determined based on measurements performed using this extension in theory. The method shows the potential to determine values for the surface and bulk absorption in future measurements. Based on a different publication by Borselli et al. (*Optics letters*, 32(20) 2007) the groundwork was laid for the use of a measurement method which separates linear and non-linear absorption terms based on properties of the thermo-optical bistability. With this method silicon and silicon nitride disks were compared. Improvements to the experimental setup and the method of analysis are suggested in order to enhance the reliability of the results of the power-varying measurement method. A third method was developed to determine the amount of removed material when silicon is oxidized by a microfabrication method and this oxide is subsequently stripped. With this stripped-oxide measurement method it is determined that the processes of the Piranha clean, the RCA-1 clean and the RCA-2 clean followed by stripping the oxide with a dilute HF solution on average remove 1.4 ± 0.3 nm, 2.3 ± 0.5 nm and 0.75 ± 0.4 nm of material.

Contents

1	Introduction	1
2	Theory	3
2.1	Optical cavities	3
2.1.1	Fabry-Pérot cavity	3
2.1.2	Microdisk cavities	4
2.2	Quality factors and loss terms	5
2.3	Theory behind the radius-varying measurement method	6
2.3.1	Surface scattering: Q_{ss} and Q_{β}	7
2.3.2	Surface absorption: Q_{sa}	7
2.3.3	Expression for \bar{u}_s for TE modes	8
2.4	Theory behind the power-varying measurement method	10
2.4.1	Non-linear absorption	10
2.4.2	Linear absorption	11
2.5	Finite-element simulations	12
2.5.1	Conversion factor for the stripped-oxide measurement method	13
3	Experimental setup and analysis	15
3.1	Experimental setup	15
3.1.1	Basic setup	15
3.1.2	Production of tapered fibers	17
3.1.3	Radius-varying measurement method	18
3.1.4	Power-varying measurement method	19
3.1.5	Stripped-oxide measurement method	22
3.2	Fabrication of the samples	22
3.3	Analysis	23
3.3.1	General analysis	23
3.3.2	Analysis of the radius-varying measurement method	23
3.3.3	Analysis of the power-varying measurement method	23
3.3.4	Analysis of the stripped-oxide measurement method	24
3.3.5	Image analysis	24
3.3.6	Uncertainty calculation	25
4	Results	27
4.1	Radius-varying measurement method	27
4.2	Power-varying measurement method	30
4.3	Stripped-oxide measurement method	32
5	Conclusion	35
A	Derivations	39
A.1	Derivation of the doublet Lorentzian transmission	39
A.2	Derivation of Q_{ss} equation	40
A.3	Derivation of Q_{β} equation	41
	Bibliography	45

Introduction

In the Gröblacher lab research is done in the field of optomechanics. This is the study of interactions between optical fields and mechanical oscillators [1]. These interactions can for example be used to accurately measure mechanical displacement [2], optically cool down mechanical systems [3] or to generate mechanical quantum states using laser light [4]. In this lab optomechanical systems, for example nanobeams [4, 5] and trampolines [6], are designed and fabricated out of silicon and silicon nitride using microfabrication methods. These methods, such as electron-beam lithography and reactive-ion etching, are indispensable for the creation of devices with sub-micrometer features, but do introduce additional optical losses, i.e. surface scattering and surface absorption.

One of the research projects in the Gröblacher lab is the optical generation of mechanical quantum states in nanobeam resonators. For this experiment surface absorption is detrimental. Due to absorption the used laser light heats up the sample introducing thermal phonons which degrade the quantum state that is generated [4]. The progress in this research subject is therefore severely limited by optical losses due to microfabrication methods.

Besides the field of optomechanics, research in nanophotonics is in great part based on microfabricated optical structures out of semiconductors too [7, 8]. Experiments in this area of research would also benefit from fabrication methods with reduced optical losses.

In order to find the fabrication processes with the least amount of optical losses, these losses must be measured and the results must be compared. Two measurement methods of optical losses using microdisk resonators are explored in this thesis. These methods are based on publications by M. Borselli et al. from 2005 and 2007 (see references [9] and [10]). Microdisks are used because they are relatively easy to fabricate and display no design-related losses. The losses that the microdisk does exhibit are either caused by the material or the fabrication process.

For the first method, the radius-varying measurement method, the losses of multiple microdisks with radii between 5 and 30 μm are investigated. Based on the radius dependence of the losses due to surface scattering and surface absorption, these terms can be separated from losses due to bulk absorption. The latter absorption term is constant with increasing radius [9].

The second method is called the power-varying measurement method and addresses the losses of a single microdisk as a function of the input power. In this way the absorption losses can be separated into terms which are linear and non-linear with the internal cavity energy [10].

A third method, the stripped-oxide measurement method, was developed during the research for this thesis. While this method is not concerned with the optical losses of the microdisks, it does use this geometry to characterize fabrication methods. Many of these processes, for example the Piranha clean and the RCA clean [11], oxidize silicon devices that are being fabricated. The device is then dipped into a diluted hydrofluoric acid (HF); this removes the silicon dioxide and by doing so the acid strips away a small layer of material. Many

optical devices are designed to work at a specific resonance wavelength and removing material changes this wavelength. The stripped-oxide measurement method can be used to determine the thickness of the material removed by the combination of an oxidizing fabrication process and the oxide stripping. This removal of material can be then be accounted for in the design process.

2

Theory

The measurement methods described in this thesis use microdisk resonators as a standardized device in order to fairly compare the loss rates of different materials. This chapter will provide theoretical backgrounds of optical cavities in general and microdisk cavities in particular, the possible loss terms of the device and the measurement methods.

2.1. Optical cavities

Before the measurement methods are introduced, the theory of optical cavities should be discussed. They can be constructed in various forms, but the general working principles are the same [13]. In this section, first the basic concept of an optical cavity is introduced by analyzing the Fabry-Pérot cavity and afterwards the microdisk cavity is more closely examined.

2.1.1. Fabry-Pérot cavity

Due to its conceptual simplicity the text book example of an optical cavity is the Fabry-Pérot cavity. It consists of two plane mirrors, parallel to and facing each other; one of them will ideally have perfect reflectivity while the other is slightly translucent to allow light to enter the cavity (see figure 2.1). The incoming light will be reflected and it will start to interfere with itself, giving rise to standing waves at certain resonant wavelengths. These standing waves are called modes. The resonance condition for these modes is $\lambda = 2Ln/(m + 1)$, where L is the length between the two mirrors, n is the refractive index of the material inside the cavity and m is 0 or a positive integer. Many wavelengths or frequencies of light satisfy this resonance condition. The distance in frequency between the modes is called the free spectral range (FSR) and is given by [1]

$$\Delta\omega_{\text{FSR}} = \omega_{m+1} - \omega_m = \frac{\pi c(m+1)}{nL} - \frac{\pi cm}{nL} = \frac{\pi c}{nL}. \quad (2.1)$$

Due to the difficulty of alignment the Fabry-Pérot cavity with two plane mirrors is rarely used for cavities of macroscopic size. In that case at least one of the plane mirrors is replaced with a concave mirror.

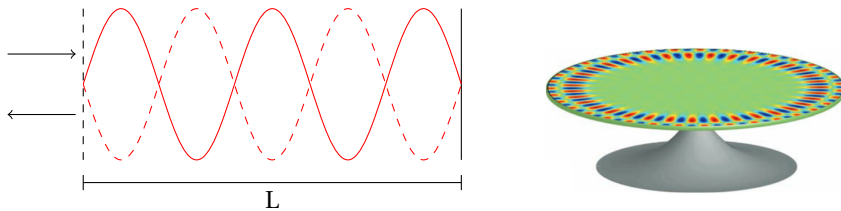


Figure 2.1: Left: Schematic representation of a resonant mode with $m = 4$ in an ideal Fabry-Pérot cavity. The vertical line on the right indicates a perfectly reflective mirror; the dashed line on the left indicates a translucent mirror, through which in- and output of light is possible as visualized by the black arrows. The mirrors are placed a distance L apart. Right: A rendering of a microdisk with a resonant mode with mode numbers $p = 2$ and $m = 35$ [12].

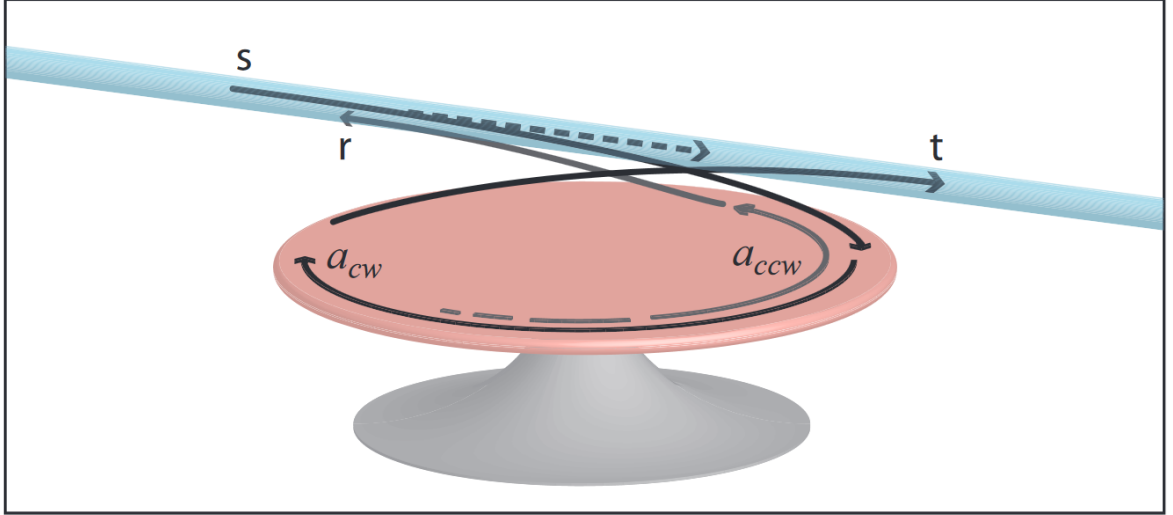


Figure 2.2: Schematic representation of the coupling between a fiber and the microdisk. The incoming light with amplitude s couples to the clockwise and counterclockwise modes, a_{cw} and a_{ccw} , which couple back to the fiber as the transmitted signal with amplitude t and reflected signal with amplitude r [12].

Probing the cavity with light close to the resonance wavelength, a dip in the amplitude of the reflected signal at the resonance frequency can be seen due to the absence or presence of destructive interference. This dip has a Lorentzian shape, of which the width and depth are governed by the losses in the system [1].

2.1.2. Microdisk cavities

When comparing a microdisk cavity with a Fabry-Pérot cavity, the main difference will be the path of the light. In a Fabry-Pérot cavity the light follows a linear path, while in a microdisk the light follows a circular path in clockwise (cw) or counterclockwise (ccw) direction. The light is contained due to total internal reflection on the disk edge [14]. Just as in the Fabry-Pérot cavity, the reflected light will interfere with itself and create standing waves; these are called whispering gallery modes. These modes do not only exist in microdisk cavities, but also in ring resonators, microspheres and -toroids. They also appear as an acoustic phenomenon from which the modes derive their name [15].

To analyze the microdisk cavity light is coupled from a waveguide into microdisks and the transmission or reflection of this light is studied, as shown in figure 2.2. For these experiments a tapered fiber was used, as shown in section 3.1.2. By using a tapered fiber with a small diameter (1 - 2 μm) and bringing the microdisk into the evanescent field of the fiber, light is coupled into the microdisk due to frustrated total internal reflection. The distance between the fiber and the disk will be in the order of 1 μm for a silicon microdisk. The degree of over- or under coupling can be regulated by making this distance smaller or larger. The modes that can be probed are determined by the polarization of the incoming light and phase matching conditions [14, 16].

In a perfectly smooth microdisk resonator each resonance consists of two degenerate modes; these modes correspond to the clockwise and counterclockwise traveling light. When there is roughness on the edge of the disk, the backscattering of the light creates a coupling between the two modes and the degeneracy is lifted. The clockwise and counterclockwise modes will form two standing wave modes, each with a Lorentzian shape in the spectrum and a resonance frequency of $\omega_0 \pm \gamma_\beta/2$. Each resonance of the microdisk is therefore considered as a doublet Lorentzian with normalized transmission [9]

$$T = \frac{|-\sqrt{P_i} + \sqrt{\gamma_{\text{ext}}/2}(a_c + a_s)|^2}{P_i}, \quad (2.2)$$

or reflection

$$R = |\sqrt{\gamma_{\text{ext}}}(a_c - a_s)|^2, \quad (2.3)$$

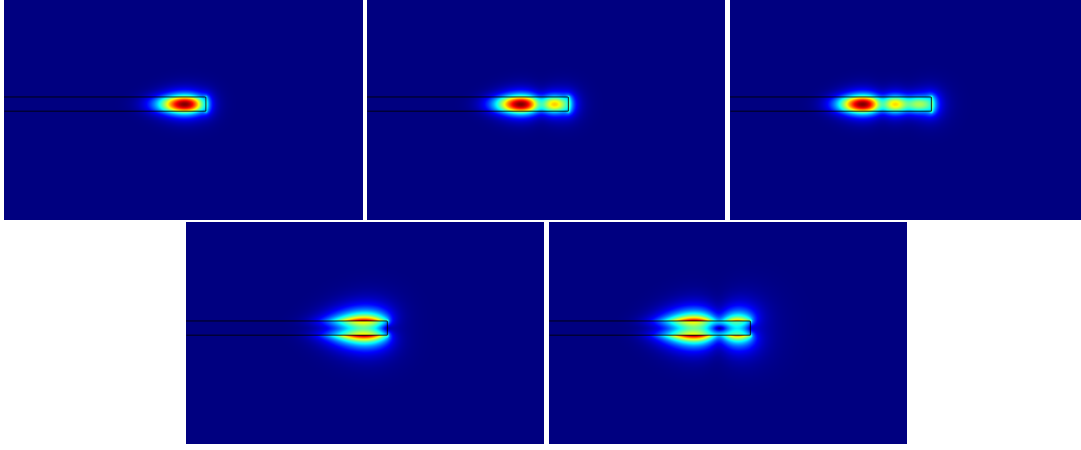


Figure 2.3: Plots of the norm of the electric field, $|\vec{E}|$, for resonant modes with different radial mode numbers. Top row: TE_{1,51}, TE_{2,46} and TE_{3,42}. Bottom row: TM_{1,34}, TM_{2,30}.

where P_i is the input power, a_c and a_s are the amplitudes of two Lorentzians in the doublet resonance and γ_{ext} is the external linewidth [10]. The amplitudes a_c and a_s are given by

$$a_c = \frac{-\sqrt{\gamma_{\text{ext}}/2}\sqrt{P_i}}{-(\gamma_c/2) + i(\Delta\omega + \gamma_\beta/2)} \text{ and } a_s = \frac{-\sqrt{\gamma_{\text{ext}}/2}\sqrt{P_i}}{-(\gamma_s/2) + i(\Delta\omega - \gamma_\beta/2)}, \quad (2.4)$$

where γ_c and γ_s are the total linewidths of each of the Lorentzian resonances and γ_β is the splitting between them. The total linewidths can be separated in an internal loss rate and the external linewidth, $\gamma_{c,s} = \gamma_{\{c,s\},i} + \gamma_{\text{ext}}$. The external loss rate, γ_{ext} , is the rate at which light leaves the cavity by coupling back into the waveguide that supplied the influx of light; the internal loss rate, $\gamma_{c,i}$ or $\gamma_{s,i}$, is determined by the rate at which the photons leave the cavity due to other reasons, for example by scattering or absorption. The notation $\Delta\omega = \omega_L - \omega_0$ corresponds to the laser detuning with ω_0 as the resonance frequency of the doublet resonance.

In the cylindrical geometry of the microdisk cavity, shown in figure 2.4, there are a number of configurations of the electromagnetic field that form a resonant mode. These configurations are labeled as either a transverse electric (TE), with $E_z = 0$, or a transverse magnetic (TM) mode, with $H_z = 0$. These two types are probed by the two orthogonal linear polarizations of the incoming light and can be separated based on their free spectral range; from simulations with COMSOL Multiphysics [17] is concluded that TE modes have a larger FSR than TM modes [16]. The modes are appointed two mode numbers; the radial mode number, p , and an azimuthal mode number, m . These are determined by the amount of anti-nodes in the $\hat{\rho}$ and the $\hat{\phi}$ direction respectively. In figure 2.3 one can see TE and TM modes with different radial mode numbers and in figure 2.1 a visualization of the azimuthal mode number can be seen. To probe the effects of the disk edge on internal Q factor most efficiently, modes with $p = 1$ will be used for the radius-varying measurement method. They are again separable based on their free spectral range. Simulations with COMSOL Multiphysics show that resonant modes with $p = 1$ have the smallest FSR in a spectrum of TE or TM modes.

2.2. Quality factors and loss terms

The goal of the radius-varying and power-varying measurement methods is measure the optical losses inside the microdisks. The quantities that are used in this thesis are the loss rate γ and the Q factor. The Q factor can be expressed in number of ways [1, 9]

$$Q = \omega \frac{U_c}{P_{\text{loss}}} = \frac{\omega}{\gamma} = \omega\tau. \quad (2.5)$$

The definition of the quality factor is the ratio between the internal cavity energy, U_c , and the power of the losses, P_{loss} , multiplied with the frequency, ω . The inverse of this ratio can also be expressed as the loss rate, γ . The quantity τ is the photon lifetime inside the cavity and is equal to $1/\gamma$. The losses in a resonator often occur through different channels which can be added up to form the total loss rate. The corresponding Q factors add reciprocally.

The internal loss rate can be split up in various components. In the case of the microdisk these are radiation losses, Q_{rad} , losses due to surface scattering, Q_{ss} , losses due to absorption, Q_{abs} :

$$\frac{1}{Q_i} = \frac{1}{Q_{\text{rad}}} + \frac{1}{Q_{\text{ss}}} + \frac{1}{Q_{\text{abs}}}. \quad (2.6)$$

Due to the very large confinement of the light inside a silicon or silicon nitride microdisk resonator, the radiation losses can be assumed negligible for the disk radii that are studied in this thesis [18].

The surface scattering losses are due to the light contained in the microdisk resonator that scatters on the index perturbations on the edge of the disk $\delta\epsilon$. These perturbations are a consequence of surface roughness or changes in the composition of the edge of the material due to the fabrication process and the etching process in particular. They are assumed to be constant in the \hat{z} -direction and can therefore be approximated by [9]

$$\delta\epsilon(\vec{r}) = \epsilon_0 \delta n^2 h \Delta r(\phi) \delta(\rho - R) \delta(z), \quad (2.7)$$

where $\delta n^2 = n_d^2 - n_0^2$, n_d and n_0 are the refractive indices of the disk and the environment, h is the microdisk thickness, ϵ_0 is the free-space electric permittivity and $\Delta r(\phi)$ is the radial surface roughness relative to the unperturbed disk radius R (see figure 2.4). The radial surface roughness $\Delta r(\phi)$ is taken to be Gaussian distributed with a correlation length L_c and an amplitude σ_r .

The losses due to absorption, γ_{abs} , can be split up in two different ways; based on the source of the absorption and based on the behavior of the absorption. Based on the source, the distinction can be made between absorption due to defects on surface and the edge of the disk, Q_{sa} , and absorption in the bulk of the material, Q_{bulk} ; these terms can be separated based with the radius-varying measurement method. Based on the behavior of the absorption, it is possible to separate Q_{abs} into a non-linear and a linear absorption term, which do and do not depend on internal cavity energy U_c respectively [19], with the power-varying measurement method.

To match the Q factor formalism that is used for the other quantities, the splitting between the doublet Lorentzian γ_β is also expressed as a Q factor

$$Q_\beta = \frac{\omega_0}{\gamma_\beta}. \quad (2.8)$$

2.3. Theory behind the radius-varying measurement method

The radius-varying measurement method is based on the fact that the whispering gallery modes will be drawn to the middle of the microdisk when the radius is increased due to increased radial confinement. This has as

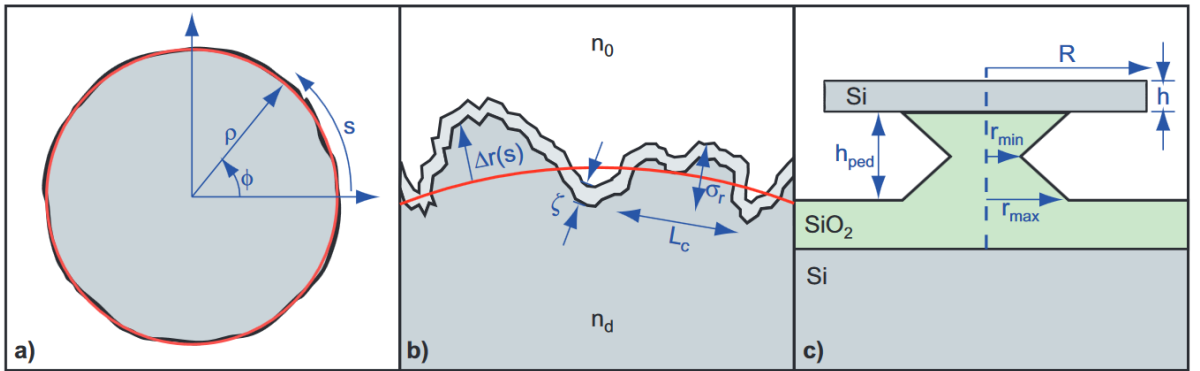


Figure 2.4: a) Coordinates of the microdisk resonator. The z axis is oriented out of plane and s indicates the arc length of the disk edge. b) Close up of microdisk edge. The red curve indicates the unperturbed disk with radius R . Variable $\Delta r(s)$ is the Gaussian distributed surface roughness with correlation length L_c and amplitude σ_r , ζ indicates the skin depth of the damages due to fabrication and variables n_d and n_0 are the refractive indices for the microdisk and the environment respectively. c) Side view of a silicon microdisk on a SiO_2 pedestal. Variable h and h_{ped} indicate the height of the microdisk and the pedestal, r_{min} and r_{max} are the radii of the hourglass shaped pedestal [9].

a consequence that the contact between the light and the disk edge diminishes with increasing radius, and that losses due to surface effects, such as surface scattering and surface absorption, will be reduced. Losses due to absorption in the bulk, Q_{bulk} , will be constant as a function of the radius. Due to the difference in the radius dependence of the bulk and the surface losses, they can be separated when analyzing microdisks of different radii [9].

To extract the values of the quality factors regarding surface scattering and absorption, expressions for Q_{ss} , Q_{β} and Q_{sa} as a function of the disk radius will be needed. The equation for Q_{β} will be fitted to the measurements of Q_{β} to extract a value for the surface roughness parameter $\sqrt{L_c}\sigma_r$. With this parameter Q_{ss} is calculated, which is then subtracted from the internal Q factor. A function, consisting of the reciprocal sum of the expression for Q_{sa} and the constant Q_{bulk} , is fitted to this reduced Q factor. From this step, values for Q_{bulk} and the surface absorption parameter $\gamma_{\text{sa}}\zeta$ are obtained. The value of this parameter determines the value of Q_{sa} . It is the product of the skin depth of the damages to the microdisk material ζ , as illustrated in figure 2.4, and the absorption loss rate in that volume γ_{sa} . In the following sections equations for Q_{β} , Q_{ss} and Q_{sa} are given together with the theoretical ideas on which they are based. Any long derivations are omitted here and can be found in appendix A. The next sections closely follow reference [9].

2.3.1. Surface scattering: Q_{ss} and Q_{β}

An equation for the surface scattering Q factor is based on the volume current method [9, 20]. This method calculates the far field radiation of the microdisk based on the polarization current originating from the random variation of the electric permittivity $\delta\epsilon$ on the disk edge due to surface roughness. In this perturbation technique the polarization current is generated by the electric field of a smooth microdisk. This far field radiation can be integrated to find the optical power lost due to scattering, which results in the Q factor [9]

$$Q_{\text{ss}} = \frac{\omega U_c}{P_{\text{rad}}} = \frac{\lambda_0^3}{\pi^{7/2} n_0 (\delta n^2)^2 V_s^2 \sum_{\hat{\eta}} \bar{u}_s(\hat{\eta}) G(\hat{\eta})} \quad (2.9)$$

where $V_s = \sqrt{RL_c} h \sigma_r$ is the volume of a typical scatterer, λ_0 is the free-space resonance wavelength, $\bar{u}_s(\hat{\eta})$, for $\hat{\eta} = \{\hat{\rho}, \hat{\phi}, \hat{z}\}$, is the normalized, spatially-averaged $\hat{\eta}$ -polarized electric field energy density at the disk edge given by

$$\bar{u}_s(\hat{\eta}) = \frac{\epsilon_0 |\vec{E}^0(\hat{\eta})|_{s,\text{avg}}^2}{\frac{1}{2} \int \epsilon^0(\vec{r}) |\vec{E}^0|^2 d\vec{r}}, \quad (2.10)$$

$G(\hat{\eta}) = \{2/3, 2, 4/3\}$ and U_c is the internal cavity energy

$$U_c = \frac{1}{2} \int \epsilon^0(\vec{r}) |\vec{E}^0|^2 d\vec{r}. \quad (2.11)$$

The parameter $\epsilon^0(\vec{r})$ is the distribution function of the electric permittivity of the unperturbed disk and \vec{E}^0 is the total electric field in the unperturbed disk, where $\vec{E}^0(\hat{\eta})$ is the component in the $\hat{\eta}$ direction. The values for the parameters of the Gaussian distribution of the surface roughness, L_c and σ_r , can be gathered from the measurement of Q_{β} . The splitting between the modes is a consequence of the backscattering rate between the clockwise and the counterclockwise traveling modes, $\gamma_{\beta}/2$. Using equation 2.7 an equation can be derived for this parameter based on a time-dependent perturbation theory, which results in an expression for Q_{β} of the form [9]

$$Q_{\beta} \equiv \frac{\omega_0}{\gamma_{\beta}} = \frac{\sqrt{2}}{\pi^{3/4} \delta n^2 V_s \sum_{\hat{\eta}} \bar{u}_s(\hat{\eta})}. \quad (2.12)$$

This equation can be fitted to the measured data for Q_{β} as a function of the microdisk radius.

2.3.2. Surface absorption: Q_{sa}

The reactive ion etching during the fabrication of the microdisks locally damages the lattice, allowing for various lattice impurities and defects. These effects in combination with the presence of dirt and residues on the microdisks cause surface absorption. The local surface absorption rate coefficient $\gamma_{\text{sa}}(\vec{r})$, is used to calculate a spatially-averaged loss coefficient according to [9]

$$\bar{\gamma}_{\text{sa}} = \frac{\int \gamma_{\text{sa}}(\vec{r}) n^2(\vec{r}) |\vec{E}(\vec{r})|^2 d\vec{r}}{\int n^2(\vec{r}) |\vec{E}(\vec{r})|^2 d\vec{r}}. \quad (2.13)$$

An approximate model for $\gamma_{sa}(\vec{r})$ would be to assume that there exists a skin depth which contains the material on the side of the disk damaged by the fabrication, ζ , where the loss rate is a constant γ_{sa} and zero elsewhere. The electric field in the numerator is therefore taken as constant over a cylindrical shell with a volume $\delta V_{sa} = 2\pi R\zeta h$. Using $n^2(\vec{r}) \simeq \epsilon_r(\vec{r}) = \epsilon^0(\vec{r})/\epsilon_0$ and $\int_{\delta V_{sa}} |\vec{E}(\vec{r})|^2 d\vec{r} \simeq \delta V_{sa} |\vec{E}(\vec{r})|_{s,avg}^2$ [9]:

$$\tilde{\gamma}_{sa} \simeq \gamma_{sa} n_{si}^2 \frac{\int_{\delta V_{sa}} |\vec{E}(\vec{r})|^2}{\int n^2(\vec{r}) |\vec{E}(\vec{r})|^2 d\vec{r}} \approx \frac{1}{2} \gamma_{sa} n_d^2 \delta V_{sa} \sum_{\hat{\eta}} \bar{u}_s(\hat{\eta}). \quad (2.14)$$

Using the Q factor definition given in equation 2.5, a quality factor for the surface absorption can be defined as [9]

$$Q_{sa} = \frac{\omega}{\tilde{\gamma}_{sa}} \simeq \frac{2c}{\lambda_0 \gamma_{sa} \zeta n_d^2 R h \sum_{\hat{\eta}} \bar{u}_s(\hat{\eta})}, \quad (2.15)$$

where c is the speed of light. The value of the unknown surface absorption parameter $\gamma_{sa}\zeta$ is determined by fitting the reciprocal sum of this expression and the constant factor Q_{bulk} to the intrinsic Q factor after the subtraction of Q_{ss} .

2.3.3. Expression for \bar{u}_s for TE modes

The equations for Q_{ss} (equation 2.9), Q_β (equation 2.12), and Q_{sa} (equation 2.15) are all dependent on the quantity $\bar{u}_s(\hat{\eta})$; the normalized, spatially-averaged $\hat{\eta}$ -polarized electric field energy density at the disk edge. To complete the derivation of analytical expressions for the aforementioned Q factors, an expression for $\bar{u}_s(\hat{\eta})$ also needs to be found. In reference [9] this is done for TM modes, but to accommodate for the measurements done with TE modes in this thesis, the theory presented in reference [9] is extended here to TE modes. The derivation starts at the definition of $\bar{u}_s(\hat{\eta})$ [9]

$$\bar{u}_s(\hat{\eta}) = \frac{\epsilon_0 |\vec{E}^0(\hat{\eta})|_{s,avg}^2}{U_c}. \quad (2.16)$$

where $|\vec{E}^0(\hat{\eta})|_{s,avg}^2$ is the electric field density averaged thin cylindrical shell of thickness δr at the edge of the disk, calculated by

$$|\vec{E}^0(\hat{\eta})|_{s,avg}^2 = \frac{1}{\delta V} \int_{R-\delta r}^{R+\delta r} \int_0^{2\pi} \int_{-h/2}^{h/2} |\vec{E}(\hat{\eta})|^2 \rho d\rho d\phi dz, \quad (2.17)$$

with $\delta V = 4\pi\delta r R h$. For a high index contrast structure, such as a silicon microdisk, the cavity mode energy can be approximated as existing only inside the cavity, reducing equation 2.11 to [9]

$$U_c = \frac{1}{2} \int \epsilon^0(\vec{r}) |\vec{E}^0|^2 d\vec{r} \approx \frac{1}{2} \epsilon_0 n_d^2 \int_0^R \int_0^{2\pi} \int_{-h/2}^{h/2} |\vec{E}^0|^2 \rho d\rho d\phi dz. \quad (2.18)$$

The integrals over ϕ and z in the numerator and the denominator of equation 2.16 are identical and drop out of the equation due to the ability to solve for the electric field with separation of variables [9]. The expression of $\bar{u}_s(\hat{\eta})$ that remains to be evaluated, contains only integrals over ρ

$$\bar{u}_s(\hat{\eta}) \approx \frac{2}{n_d^2 \delta V} \frac{\int_{R-\delta r}^{R+\delta r} |E_\eta|^2 \rho d\rho}{\int_0^R |E|^2 \rho d\rho}, \quad (2.19)$$

where E_η is the magnitude of the E-field in the $\hat{\eta}$ -direction, and where $|E|^2$ is equal to $|\vec{E}^0|^2$ with any ρ and z dependence integrated out. The integral over the thin shell in the numerator of equation 2.19 is solved approximately by taking the integrand as a constant value $[|E_\eta|^2 \rho]_{\rho=R}$ over the interval $R - \delta r \leq \rho \leq R + \delta r$

$$\bar{u}_s(\hat{\eta}) \approx \frac{2}{n_d^2 \delta V} \frac{2\delta r R [|E_\eta|^2]_{\rho=R}}{\int_0^R |E|^2 \rho d\rho} = \frac{[|E_\eta|^2]_{\rho=R}}{n_d^2 \pi h \int_0^R |E|^2 \rho d\rho}. \quad (2.20)$$

Now only the integral in the denominator remains to be solved, for this an expression for the electric field in the $\hat{\rho}$ and $\hat{\phi}$ direction is needed.

The electric field for TE modes is given by $\vec{E}^0 \propto E_\rho \hat{\rho} + E_\phi \hat{\phi}$. The field components E_ρ and E_ϕ are derived from the magnetic field in the \hat{z} -direction [21]

$$H_z \propto \begin{cases} J_m(k_0 \bar{n} \rho) e^{im\phi}, & \rho \leq R \\ J_m(k_0 \bar{n} R) e^{-\alpha(\rho-R)} e^{im\phi}, & \rho > R \end{cases} \quad (2.21)$$

with k_0 the free-space wave vector, m the azimuthal mode number, $\alpha = k_0 \sqrt{\bar{n}^2 - n_0^2}$ and \bar{n} the effective refractive index, according to the equations [22]

$$E_\rho = \frac{i}{k_0 \bar{n}^2 \rho} \frac{\partial H_z}{\partial \phi} \sim \frac{-m}{k_0 \bar{n}^2 \rho} J_m(k_0 \bar{n} \rho) e^{im\phi} \quad |E_\rho|^2 \sim \left(\frac{m}{k_0 \bar{n}^2 \rho} \right)^2 [J_m(k_0 \bar{n} \rho)]^2, \quad (2.22a)$$

$$E_\phi = -\frac{i}{k_0 \bar{n}^2} \frac{\partial H_z}{\partial \rho} \sim -\frac{i}{k_0 \bar{n}^2} \frac{\partial}{\partial \rho} [J_m(k_0 \bar{n} \rho)] e^{im\phi} \quad |E_\phi|^2 \sim \left(\frac{1}{k_0 \bar{n}^2} \right)^2 \left(\frac{\partial}{\partial \rho} [J_m(k_0 \bar{n} \rho)] \right)^2, \quad (2.22b)$$

with the assumption that \bar{n} does not carry a dependence on ρ or ϕ in the disk. The magnitude of the total electric field is given by

$$|E|^2 = |E_\rho|^2 + |E_\phi|^2. \quad (2.23)$$

The effective refractive index can be calculated with the slab mode calculations [9], by solving the equations [23]

$$\begin{aligned} \frac{qh}{2} &= \frac{dh}{2} \tan\left(\frac{dh}{2}\right) \\ \left(\frac{qh}{2}\right)^2 + \left(\frac{dh}{2}\right)^2 &= (n_d^2 - n_0^2) k_0^2 \left(\frac{h}{2}\right)^2 \end{aligned}$$

simultaneously for q or d for the TE modes. The effective index can then be calculated from these variables with [23]

$$\begin{aligned} \bar{n}^2 &= n_d^2 - \left(\frac{d}{k_0}\right)^2 \\ \bar{n}^2 &= n_0^2 + \left(\frac{q}{k_0}\right)^2. \end{aligned}$$

This results in an effective refractive index \bar{n} of 2.91 for a silicon microdisk with $h = 250$ nm, $n_0 = 1$ and $n_d = 3.48$ with a wavelength of 1550 nm. By applying the boundary conditions at $\rho = R$ for the H_z and the E_ϕ field for the TE modes, the transcendental equation [9]

$$k_0 \bar{n} J_{m+1}(k_0 \bar{n} R) = \left(\frac{m}{R} + \eta \alpha\right) J_m(k_0 \bar{n} R), \quad (2.26)$$

with $\eta = \bar{n}^2 / n_0^2$, can be derived. By applying the recurrence relations [24]

$$\frac{J_m(x)}{x} = \frac{1}{2} (J_{m-1}(x) + J_{m+1}(x)) \quad (2.27a)$$

$$\frac{dJ_m(ax)}{dx} = \frac{1}{2} a (J_{m-1}(ax) - J_{m+1}(ax)) \quad (2.27b)$$

the following equations are derived for $|E_\rho|^2$ and $|E_\phi|^2$:

$$|E_\rho|^2 \sim \frac{1}{4\bar{n}^2} (J_{m-1}(k_0 \bar{n} \rho) + J_{m+1}(k_0 \bar{n} \rho))^2 \quad (2.28a)$$

$$|E_\phi|^2 \sim \frac{1}{4\bar{n}^2} (J_{m-1}(k_0 \bar{n} \rho) - J_{m+1}(k_0 \bar{n} \rho))^2. \quad (2.28b)$$

The equations 2.23, 2.28a and 2.28b are entered into equation 2.20 and by solving the integrals and simplifying the resulting expressions with Wolfram Mathematica [25], the following equations are derived:

$$\bar{u}_s(\hat{\rho}) = \frac{1}{n_d^2 h \pi} \frac{k_0 \bar{n} x [J_{m-1}(x) + J_{m+1}(x)]^2}{2 [(2m + x^2) J_m(x)^2 - 2(m + 1) x J_m(x) J_{m+1}(x) + x^2 J_{m+1}(x)^2]} \quad (2.29a)$$

$$\bar{u}_s(\hat{\phi}) = \frac{1}{n_d^2 h \pi} \frac{k_0 \bar{n} x [J_{m-1}(x) - J_{m+1}(x)]^2}{2 [(2m + x^2) J_m(x)^2 - 2(m + 1) x J_m(x) J_{m+1}(x) + x^2 J_{m+1}(x)^2]} \quad (2.29b)$$

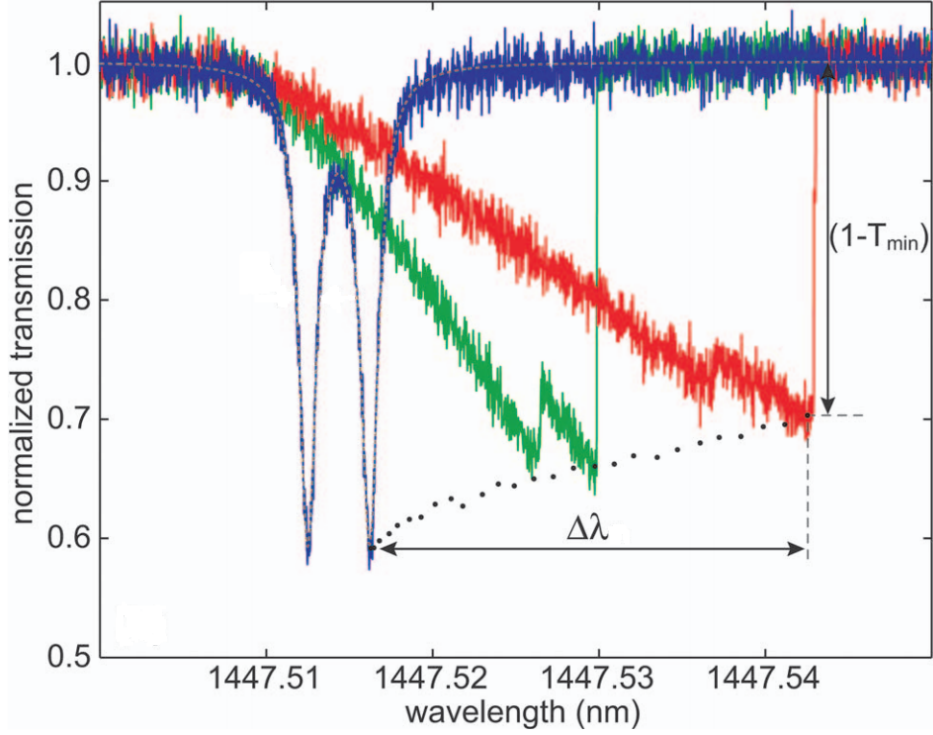


Figure 2.5: Plots of the normalized doublet resonances of a 10 μm radius silicon microdisk measured at 4 μW , 50 μW , and 100 μW for the blue, green and red curves respectively. Indicated in this figure are the resonance wavelength shift $\Delta\lambda$ between the blue and red curves and the quantity $1 - T_{\min}$ for the red curve [10].

with $x = k_0 \bar{n} R$ for ease of notation. Using equation 2.26, equations 2.29a and 2.29b can be rewritten containing solely Bessel functions of order m . To remove any dependence on the azimuthal mode number m , it can be approximated by $m \approx k_0 \bar{n} R$ [21], resulting in the equations

$$\bar{u}_s(\hat{\rho}) \approx \frac{1}{n_d^2 h \pi} \frac{2\bar{k}^2}{\bar{\alpha}^2 R^2 - 2\bar{\alpha} R} \quad (2.30a)$$

$$\bar{u}_s(\hat{\phi}) \approx \frac{1}{n_d^2 h \pi} \frac{[\bar{k}(2\bar{\alpha} R - 1) + \bar{\alpha}(\bar{\alpha} R - 1)]^2}{2\bar{\alpha} R(\bar{\alpha} R - 2)[(\bar{k} + \bar{\alpha})R - 1]^2} \quad (2.30b)$$

with $\bar{k} = k_0 \bar{n}$ and $\bar{\alpha} = \alpha \eta$ for ease of notation. Entering these equations into 2.9, 2.12 and 2.15 results into analytic expressions for Q_{ss} , Q_β and Q_{sa} .

2.4. Theory behind the power-varying measurement method

The power-varying measurement method determines the linear and the non-linear absorption by exploiting the properties of the thermally induced optical bistability [10]. By increasing the amount of laser power that is put into the device, the system heats up and, due to the thermo-optic effect, the transmission resonance shape changes. From the difference in the depth of the transmission dip at the resonance wavelength with increasing input power the non-linear absorption is derived. By combining this data with the shift in the resonance wavelength as a function of input power, the linear absorption rate can also be discovered without any prior knowledge about the material or geometry. See figure 2.5 for an example of some measurements done while using the power-varying measurement method [10].

2.4.1. Non-linear absorption

In order to extract the value of the non-linear absorption rate γ_{nla} an expression for γ_{nla} as a function of the transmission dip T_{\min} is needed. This derivation is based on reference [10], which gives the equation for the non-linear absorption based on T_{\min} for a singlet resonance. The approach used in that paper is applied here to a doublet resonance. The starting point is equation 2.2 in combination with equation 2.4. The assumption

is made that γ_{ext} and γ_{β} do not change with increased laser power [10], and the total loss rates γ_c and γ_s are taken to be equal and are noted as γ_t . With the knowledge that P_i , γ_{ext} , γ_t , γ_{β} and $\Delta\omega$ are real variables and that of these variables P_i , γ_{ext} , γ_t and γ_{β} are positive it is possible to rewrite equation 2.2 as

$$T = \frac{(-2\gamma_{\text{ext}}\gamma_t + \gamma_t^2 + \gamma_{\beta}^2)^2 + 8(2\gamma_{\text{ext}}^2 - 2\gamma_{\text{ext}}\gamma_t + \gamma_t^2 - \gamma_{\beta}^2)\Delta\omega^2 + 16\Delta\omega^4}{(\gamma_t^2 + (\gamma_{\beta} - 2\Delta\omega)^2)(\gamma_t^2 + (\gamma_{\beta} + 2\Delta\omega)^2)}. \quad (2.31)$$

In order to convert equation 2.31 into an expression for the depth of the transmission T_{min} , it is necessary to look at the value of T at the frequency of one of the Lorentzians that make up the doublet resonance. This frequency corresponds to a laser detuning of $\Delta\omega = \pm\gamma_{\beta}/2$; because of the fact that the detuning only appears in even powers in the equation, it does not matter which sign is picked. When this substitution is made, the equation is transformed into

$$T_{\text{min}} = \frac{(\gamma_{\text{ext}} - \gamma_t)^2}{\gamma_t^2} + \frac{\gamma_{\text{ext}}(3\gamma_{\text{ext}} - 2\gamma_t)}{\gamma_t^2 + 4\gamma_{\beta}^2}. \quad (2.32)$$

At very low power there is no non-linear absorption; this value of the total linewidth is named the cold cavity absorption γ_{cold} . The total linewidth at any power is split up in a cold cavity linewidth and an added non-linear absorption term $\gamma_t = \gamma_{\text{cold}} + \gamma_{\text{nla}}$. The non-linear absorption rate γ_{nla} is normalized by dividing it by the γ_{cold} [10]. These two substitutions produce the equation

$$T_{\text{min}} = \frac{(\gamma_{\text{cold}} - \gamma_{\text{ext}} + \gamma_{\text{cold}}\gamma'_{\text{nla}})^2}{(\gamma_{\text{cold}} + \gamma_{\text{cold}}\gamma'_{\text{nla}})^2} + \frac{\gamma_{\text{ext}}(3\gamma_{\text{ext}} - 2\gamma_{\text{cold}}(1 + \gamma'_{\text{nla}}))}{(\gamma_{\text{cold}} + \gamma_{\text{cold}}\gamma'_{\text{nla}})^2 + 4\gamma_{\beta}^2}. \quad (2.33)$$

The solution of this equation for γ'_{nla} can be expressed as the positive real root of the equation

$$ax^4 + bx^3 + cx^2 + dx + e = 0, \quad (2.34)$$

with the coefficients

$$\begin{aligned} a &= \gamma_{\text{cold}}^4 T_{\text{min}} - \gamma_{\text{cold}}^4, \\ b &= -4\gamma_{\text{cold}}^4 + 4\gamma_{\text{cold}}^3\gamma_{\text{ext}} + 4\gamma_{\text{cold}}^4 T_{\text{min}}, \\ c &= -6\gamma_{\text{cold}}^4 + 12\gamma_{\text{cold}}^3\gamma_{\text{ext}} - 4\gamma_{\beta}^2\gamma_{\text{cold}}^2 - 4\gamma_{\text{cold}}^2\gamma_{\text{ext}}^2 + 6\gamma_{\text{cold}}^4 T_{\text{min}} + 4\gamma_{\beta}^2\gamma_{\text{cold}}^2 T_{\text{min}}, \\ d &= -4\gamma_{\text{cold}}^4 + 12\gamma_{\text{cold}}^3\gamma_{\text{ext}} - 8\gamma_{\beta}^2\gamma_{\text{cold}}^2 - 8\gamma_{\text{cold}}^2\gamma_{\text{ext}}^2 + 8\gamma_{\beta}^2\gamma_{\text{cold}}\gamma_{\text{ext}} + 4\gamma_{\text{cold}}^4 T_{\text{min}} + 8\gamma_{\beta}^2\gamma_{\text{cold}}^2 T_{\text{min}}, \\ e &= -\gamma_{\text{cold}}^4 + 4\gamma_{\text{cold}}^3\gamma_{\text{ext}} - 4\gamma_{\beta}^2\gamma_{\text{cold}}^2 - 4\gamma_{\text{cold}}^2\gamma_{\text{ext}}^2 + 8\gamma_{\beta}^2\gamma_{\text{cold}}\gamma_{\text{ext}} - 4\gamma_{\beta}^2\gamma_{\text{ext}}^2 + \gamma_{\text{cold}}^4 T_{\text{min}} + 4\gamma_{\beta}^2\gamma_{\text{cold}}^2 T_{\text{min}}, \end{aligned}$$

under the condition that

$$T_{\text{min}}|_{\gamma_{\text{nla}}=0} < T_{\text{min}} < 1. \quad (2.35)$$

The root of a fourth-order polynomial can be solved analytically and from this expression an equation for the error in γ'_{nla} is derived. The non-linear absorption γ'_{nla} will be plotted as function of the internal cavity energy $U_c = P_d/\gamma_t$, where $P_d = (1 - T_{\text{min}})P_i$ is the dropped power and $\gamma_t = \gamma_c(1 + \gamma'_{\text{nla}})$.

2.4.2. Linear absorption

The linear absorption will be determined based on the resonance wavelength shift $\Delta\lambda$ due to the increased input power P_i . This input power is the amount of light that is sent towards the microdisk resonator; of this light, only the dropped power $P_d = (1 - T_{\text{min}})P_i$ will actually be coupled into the cavity at the resonance wavelength. Of this dropped power, only the part of the light that is absorbed will cause a resonance wavelength shift due to the thermo-optic effect [10]. For small temperature changes, the expectation is that $\Delta\lambda$ will be linearly proportional the absorbed power. All other thermal or thermo-optic effects are gathered into a factor C and the resonance wavelength shift is expressed as [10]

$$\Delta\lambda = C \left(\frac{\gamma_{\text{abs}}}{\gamma_t} \right) P_d = C \left(\frac{\gamma'_{\text{la}} + \gamma'_{\text{nla}}(P_d)}{1 + \gamma'_{\text{nla}}(P_d)} \right) P_d. \quad (2.36)$$

In the rightmost part of this equation the photon absorption rate is split up into a linear and non-linear part. If the non-linear absorption rate is not a constant function of P_d , it is possible to obtain γ'_{la} and the constant

C by fitting equation 2.36 to the measurements of $\Delta\lambda$ as a function of P_d .

In order to corroborate the measurements of the power-varying measurement method, it is possible to calculate a value for parameter C and obtain γ'_{la} using this calculated value [9]. Based on material properties of the disk, such as the refractive index n_d and the thermo-optic coefficient dn/dT , and the thermal resistance of the pedestal R_{th} , a value for C can be calculated as [9]

$$C_{calc} = \left(\frac{\frac{dn}{dT} R_{th} \lambda_0}{n_d} \right), \quad (2.37)$$

with

$$R_{th} = \frac{h_{ped}}{\kappa \pi r_{max} r_{min}}, \quad (2.38)$$

where κ is the thermal conductivity of the pedestal material and h_{ped} is the height of the pedestal. The parameters r_{max} and r_{min} are the radii of the pedestal shape as seen in figure 2.4. With a value of C_{calc} it is possible to derive the absorbed power from the resonance wavelength shift [9]

$$P_{abs} = \frac{\Delta\lambda}{C_{calc}}. \quad (2.39)$$

When this absorbed power is plotted against the internal cavity energy U_c , the linear absorption rate γ_{la} can be obtained through the cubic polynomial fit of $P_{abs} = aU_c^3 + bU_c^2 + \gamma_{la}U_c$.

2.5. Finite-element simulations

In support of the measurements a number of finite-element simulations are performed with the software COMSOL Multiphysics [17]. The simulations were eigenfrequency calculations of the microdisk performed in the region of frequencies matching the experiments. In order to reduce the computing time to a manageable level a 2D axisymmetric model is used instead of a full three-dimensional model. This is possible due to the rotational symmetry of microdisk resonator. The ϕ -dependence of the modes corresponding to the eigenfrequencies is of the form $e^{im\phi}$, where m is the azimuthal mode number. To obtain the eigenfrequencies of the modes in a certain frequency range the eigenfrequency calculations have to be repeated for a range of values of m [16]. The simulation geometry is shown in figure 2.6a. The microdisk is surrounded by an air box and perfectly matched layers to replicate an environment filled with air of infinite size. The mesh elements have a maximum size of $\lambda/5$ in every material.

If only the TE or the TM modes are required to be calculated, the symmetry of the microdisk and the modes in the $\rho - \phi$ plane can be exploited to reduce the computation time even further. In order to achieve this the axisymmetric geometry is split in half in the middle of the disk and the boundary conditions $\hat{n} \times \vec{H} = \vec{0}$ and

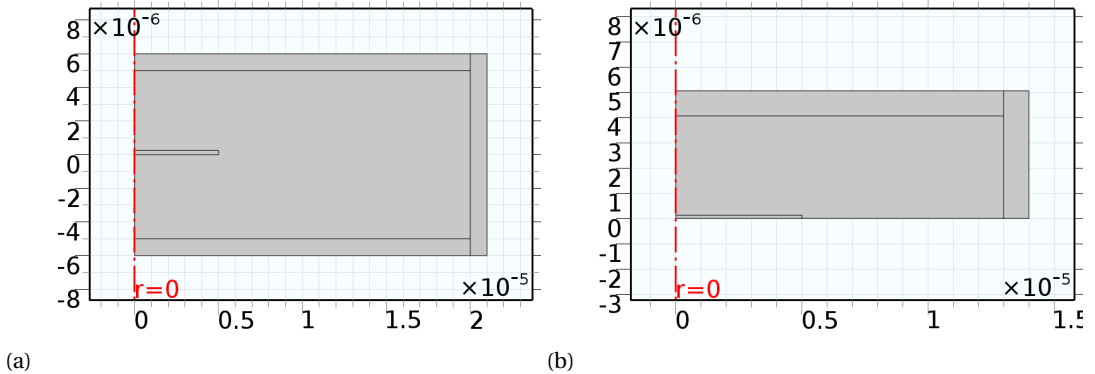


Figure 2.6: Axisymmetric geometries used in the finite-element simulations. The red-dashed line shows the axis around which the rotational symmetry is exploited; the horizontal and vertical axis show the ρ and z coordinate respectively in meters. Figure 2.6a produces both TE and TM modes when used in an eigenfrequency calculation; with figure 2.6b eigenfrequency calculation can be used to obtain resonant frequencies for TE modes or TM modes when the boundary conditions $\hat{n} \times \vec{H} = \vec{0}$ or $\hat{n} \times \vec{E} = \vec{0}$ respectively are applied to the line $z = 0$.

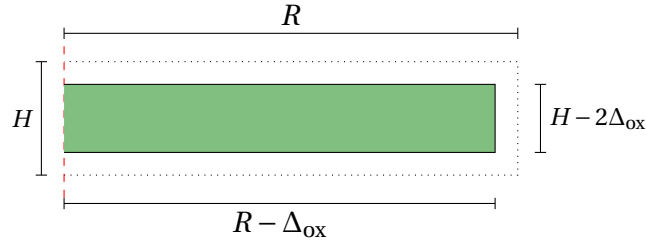


Figure 2.7: Schematic representation of the geometry used in the COMSOL simulations for the conversion factor used in the stripped-oxide measurement method. The red, dashed line indicates the axis around which the rotational symmetry is taken.

$\hat{n} \times \vec{E} = \vec{0}$ are applied on this symmetry line for the TE and TM modes respectively. The geometry for these calculations is shown in figure 2.6b.

2.5.1. Conversion factor for the stripped-oxide measurement method

In this thesis a method is discussed to determine the thickness of the layer of silicon that gets oxidized and stripped away when applying a cleaning fabrication process, e.g. a Piranha clean, and subsequently dipping the sample in a dilute HF solution. This method is based on the relation between the resonance wavelength of the microdisks and their dimensions; when the disk gets smaller, the resonance wavelength shifts to the blue side. The relation between the absolute value of the resonance wavelength shift, $|\Delta\lambda|$, and the amount of stripped oxidized material Δ_{ox} is defined as

$$f_{\text{conv}} = \frac{|\Delta\lambda|}{\Delta_{\text{ox}}}. \quad (2.40)$$

This conversion factor is calculated using COMSOL Multiphysics [17]. A microdisk is simulated with radius $R - \Delta_{\text{ox}}$ and height $H - 2\Delta_{\text{ox}}$, as shown in figure 2.7. The factor Δ_{ox} is incorporated double in the height because of oxidation on both the top and bottom of the disk. The measurements were preformed on a microdisk with a radius of $R = 5 \mu\text{m}$ and a height of $H = 250 \text{ nm}$; the simulations have therefore also been done on a geometry with these dimensions. A parametric sweep is performed that changes $\Delta_{\text{ox}} = 0$ to 10 nm in steps of 1 nm and for each value of Δ_{ox} the eigenfrequencies of the microdisk in a certain frequency range are determined. The data presented in this section is based on TE modes with a radial mode of $\rho = 1$ to match the measurements. From the resonance wavelengths for the various values of Δ_{ox} a conversion factor can be found between the wavelength shift of the resonances and the amount of material that was removed.

Due to the fact that a nanometer of stripped material relatively becomes larger when the microdisk gets a smaller radius, the conversion factor becomes larger if more oxidized material is stripped. In the regime shown in this graph the conversion factor can be interpreted as a linear function of Δ_{ox} . In figure 2.8 can also be seen that there is a dependence of the coefficients of this linear function on the resonance wavelength at $\Delta_{\text{ox}} = 0 \text{ nm}$, λ_s . When these coefficients are plotted against these resonance wavelengths, it can be seen that they too show a linear dependence. The equation for the conversion factor ends up to be

$$f_{\text{conv}} = \psi(\lambda_s)\Delta_{\text{ox}} + \nu(\lambda_s), \quad (2.41a)$$

$$\psi(\lambda_s) = a\lambda_s + b, \quad (2.41b)$$

$$\nu(\lambda_s) = c\lambda_s + d, \quad (2.41c)$$

Table 2.1: Coefficients for the wavelength dependency of the conversion factor for the stripped-oxide measurement method as used in equations 2.41b and 2.41c.

	Coefficient
a	$(2.58 \pm 0.01) \times 10^{-5} \text{ nm}^{-2}$
b	$(-8.1 \pm 0.2) \times 10^{-12} \text{ m/nm}^2$
c	$(3.12 \pm 0.01) \times 10^{-3} \text{ nm}^{-1}$
d	$(-2.14 \pm 0.02) \times 10^{-9} \text{ m/nm}$

where $\psi(\lambda_s)$ and $v(\lambda_s)$ are wavelength dependent, linear functions with the coefficients a, b, c and d. The values for these coefficients can be found in table 2.1.

If a microdisk is reused multiple times for the stripped-oxide measurement method, then f_{conv} will have a different value for each measurement depending on the amount of material previously stripped. This is shown in the plot on the left hand side of figure 2.8. This effect can be accounted for by introducing the amount of material stripped from the disk before the measurements χ into the equation as follows;

$$f_{\text{conv}}(\Delta_{\text{ox}}, \lambda_s, \chi) = \psi(\lambda_s)(\Delta_{\text{ox}} + \chi) + v(\lambda_s) = \psi(\lambda_s)\Delta_{\text{ox}} + \psi(\lambda_s)\chi + v(\lambda_s). \quad (2.42)$$

Due to the shift in resonance wavelength due to the material stripped beforehand, the current resonance wavelength λ_c is different than the resonance of the unstripped disk λ_s . The correct value of λ_s will then be

$$\begin{aligned} \lambda_s &= \lambda_c + f_{\text{conv}}(\chi, \lambda_s, 0)\chi \\ &= \lambda_c + [(a\lambda_s + b)\chi + c\lambda_s + d\chi]\chi \\ &= \frac{\lambda_c + b\chi^2 + d\chi}{1 - a\chi^2 - c\chi}. \end{aligned} \quad (2.43)$$

To ultimately go from a value of $|\Delta\lambda|$ to Δ_{ox} , the equation to solve is

$$\begin{aligned} f_{\text{conv}}\Delta_{\text{ox}} &= |\Delta\lambda| \\ [\psi(\lambda_s)(\Delta_{\text{ox}} + \chi) + v(\lambda_s)]\Delta_{\text{ox}} &= |\Delta\lambda| \\ \psi(\lambda_s)\Delta_{\text{ox}}^2 + [\psi(\lambda_s)\chi + v(\lambda_s)]\Delta_{\text{ox}} - |\Delta\lambda| &= 0. \end{aligned} \quad (2.44)$$

The value of Δ_{ox} will be the positive root of this quadratic equation

$$\Delta_{\text{ox}} = \frac{-[\psi(\lambda_s)\chi + v(\lambda_s)] + \sqrt{[\psi(\lambda_s)\chi + v(\lambda_s)]^2 + 4\psi(\lambda_s)|\Delta\lambda|}}{2\psi(\lambda_s)}. \quad (2.45)$$

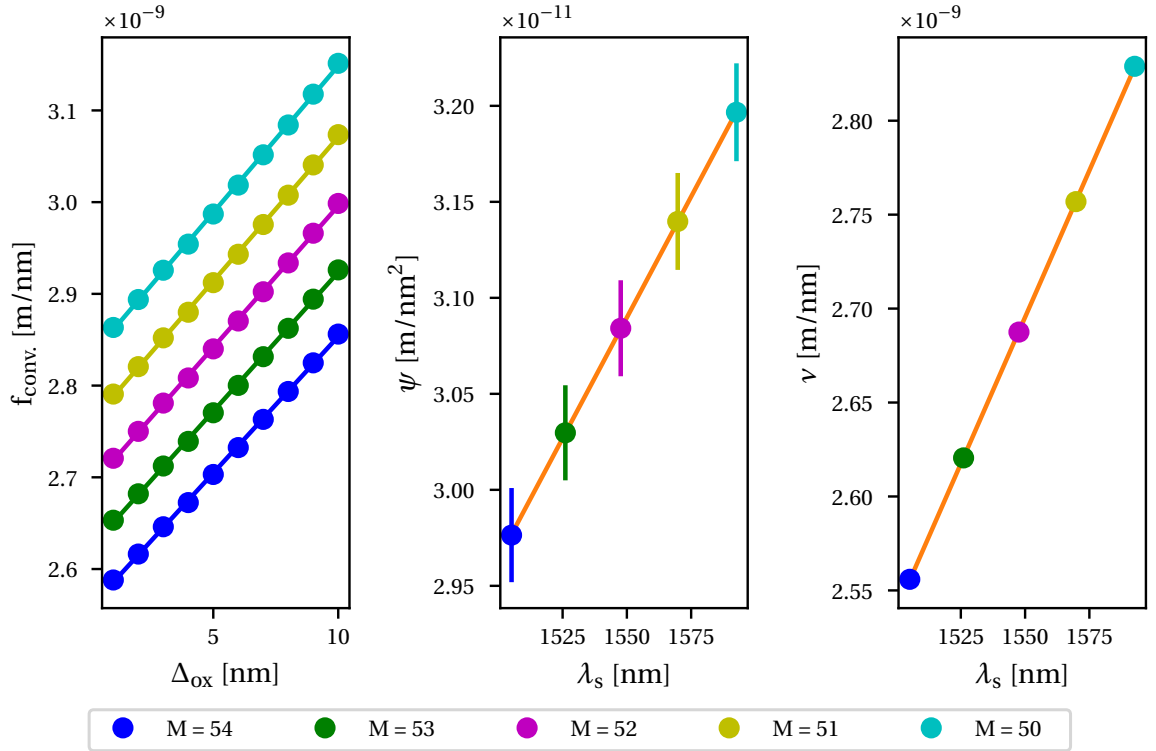


Figure 2.8: The graph on the left shows the linear dependence of the conversion factor f_{conv} on Δ_{ox} for the azimuthal mode numbers $M = 50$ to 54 . The two graphs on the right show the linear coefficients of the plots on the left as a function of starting wavelength.

Experimental setup and analysis

In this thesis three measurement methods are mentioned, each with their own measured quantities. In this chapter the experimental setup for each type of measurement and the corresponding method of data analysis will be discussed. In section 3.2 the fabrication of the samples is described.

3.1. Experimental setup

The experimental setups for the various measurements are very similar to each other and could be regarded as variations on a basic setup. A schematic overview of the fiber circuit can be found in figure 3.1. The components indicated by a red box are additions to the basic setup to allow for the power-varying measurement method. The parts surrounded by a gray box, a 99:1 beam splitter and a wave meter, are used in the stripped-oxide measurement method. Why they are added and what they do in these scenarios, is explained in sections 3.1.4 and 3.1.5 respectively.

3.1.1. Basic setup

Fiber optics

The setup is completely fiber based and has a Santec TSL-510 laser at its heart. The laser is a tunable external cavity laser based on the Littman-Metcalf configuration [26, 27]. The diode-generated laser beam is reflected off a diffraction grating; the light with the desired wavelength is scattered back, while the other laser light is sent towards a mirror and reflected back at the diffraction grating. By moving this mirror the wavelength of the output light can be controlled. For a schematic overview of this setup (see figure 3.2). The laser has a built in possibility to move this mirror automatically; while this method allows for a large scanning range, it has a relatively large resolution. The wavelength range of this coarse scanning method is maximally from 1500 to 1630 nm. The laser also offers a way to sweep the wavelength of the output in a more precise way by applying an external voltage V_L . This voltage in the range of ± 0.95 V is applied to the device, which will be sent to a piezoelectric element that moves the mirror. The rate of wavelength change is typically -40 pm/V [26]. By applying a range of narrowly stepped voltages, the laser wavelength can be varied in small increments. The resolution of the fine scan is approximately 2 fm. The laser is controlled by a computer through either an Ethernet connection or by using a National Instruments Digital Acquisition (DAQ) card, using code that was developed based on existing software.

In order to control the polarization and the amplitude of the light that is incident on the disk, a fiber polarization controller (FPC) and a Sercalo VP1-9N variable optical attenuator (VOA) are placed right after the laser. By applying a voltage between 0 and 5 V to the VOA, the attenuation can be varied between 0 and 40 dB [28]. This voltage, and therefore the laser power in the circuit, is controlled by a computer using a National Instruments DAQ card.

When the correct polarization and amplitude are dialed in, the light is sent through a 50:50 beam splitter where it can take two paths. One of these paths goes towards the disk, where the light gets sent through a tapered fiber where it couples to the microdisk. At the end of this path the intensity of the transmitted light is measured using a photodiode. This signal is then amplified 2×10^2 times by a Stanford Research SR560

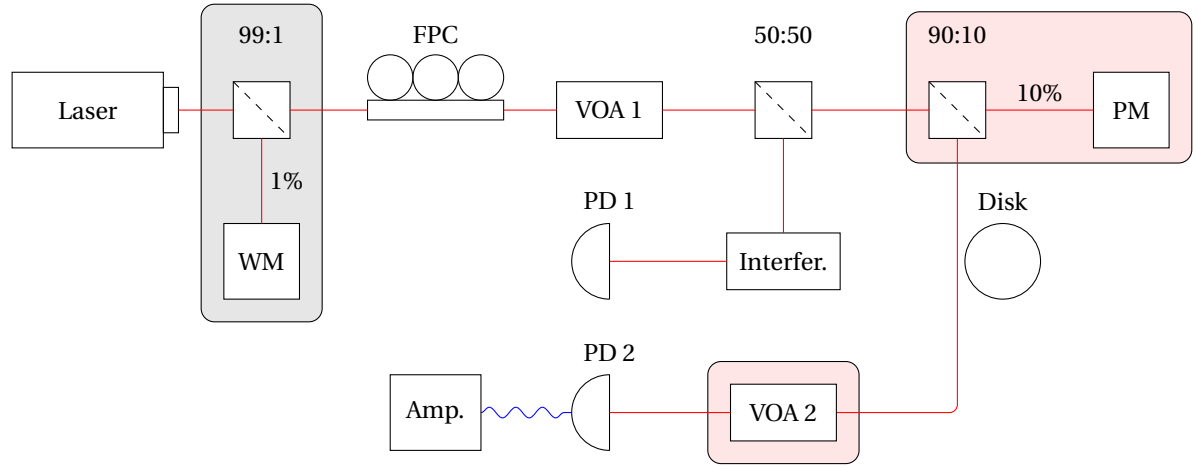


Figure 3.1: Schematic of the measurement setup. The areas that are shaded red are additions to the basic setup for the power-varying measurements, those shaded gray are components necessary for the stripped-oxide measurement method.

amplifier and filtered by a 12 dB low pass filter with a cut-off frequency of 3 kHz inside the same machine. The electrical signal that is produced by the amplifier is recorded by a computer through a National Instruments DAQ card. Due to the timing of the experiments and the acquisition of the amplifier it was not used for the measurements done with the radius-varying measurement method.

The other arm of the 50:50 beam splitter goes towards an Mach-Zehnder interferometer of which the outgoing laser intensity is again measured by a photodiode and recorded by a National Instruments DAQ card. This interferometer is used to accurately determine the linewidth of a fine scanned resonance or wavelength shifts between consecutive measurements. The free spectral range of the Mach-Zehnder interferometer was calibrated using a High Finesse WS-6 wave meter before using it in the measurement setup.

Sample stage

The investigated microdisks are situated on a microchip. In order to evanescently couple light into these microdisks, the tapered fiber and the disk have to be positioned a couple hundred nanometers apart [16]. The tapered fiber is placed in a U-mount (see figure 3.3), and can roughly be positioned by using micrometer-precision manual stages. The microchip is placed on a Mechanics MX 35 stage, which is controlled by the Mechanics CU30 controller. This combination allows the microchip to be positioned in three dimensions with a precision of approximately 30 nm. The Mechanics CU30 is connected to a computer via a USB connection and controlled by either Mechanics software or a LabVIEW program based on an existing driver. To align

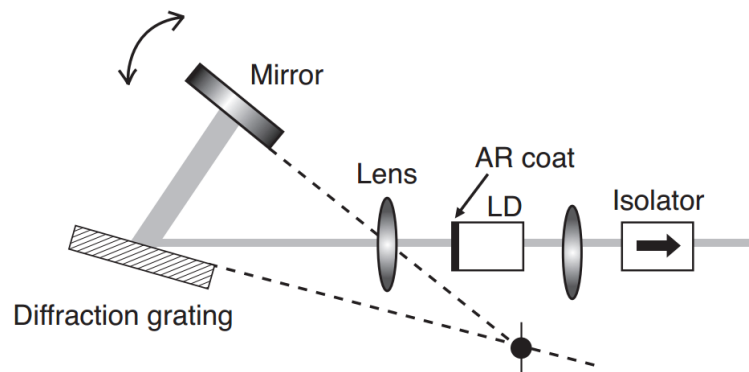


Figure 3.2: Inner workings of the Santec TSL-510 laser. The generation of the light starts at the laser diode (LD) with an anti-reflection coating (AR coat). This light is sent to a diffraction grating where based on the mirror position the desired wavelength gets reflected back [26].

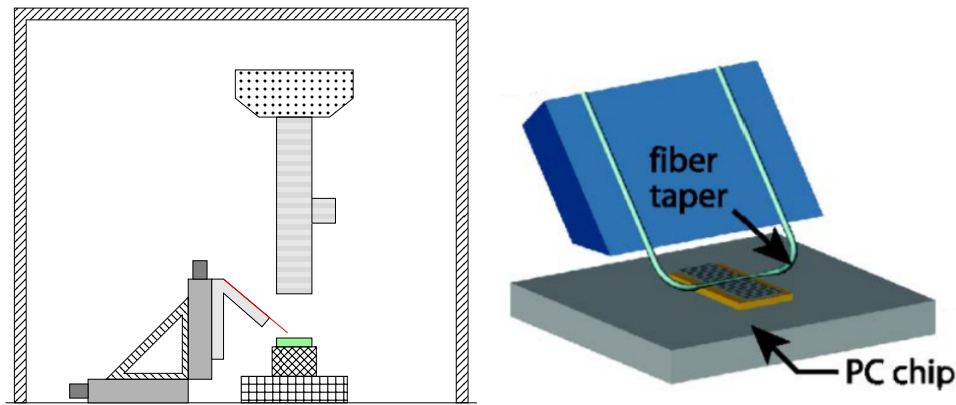


Figure 3.3: Left figure: Drawing of the experimental setup. In the right column can be seen, from bottom to top, the tip-tilt and rotation stage, the Mechanics MX 35 stage, the investigated sample, the Navitar zoom system with the objective attached and the Nikon D5200 camera. The feature on the right side of the Navitar system is the input for the fiber optic illuminator. On the left side two manual stages are seen connected with a triangle piece. To these stages a U-mount piece can be seen with the fiber, draw in red. The whole system is placed in a nitrogen purged plexiglass enclosure. Not shown is a mount for the imaging system. Right figure: Image of the U-mount piece on which the tapered fiber is mounted, shown here measuring a photonic crystal (PC) chip [29].

the tapered fiber and the chip, the Mechanics MX 35 stage is placed on a tip-tilt stage and a rotation stage. To make sure that the fiber and the microdisks are situated correctly a microscope setup is implemented to visually check the alignment of the fiber and the microchip. This imaging setup consists of a Navitar Zoom 6000 system with a Mitutoyo M Plan Apo 50x objective. A Nikon D5200 dSLR body is used as an imaging sensor and the lighting is provided by a fiber optic illuminator through the Navitar zoom system. A drawing of the setup can be seen in figure 3.3.

Measurement routine

The measurement routine starts by performing a coarse scan of the microdisk over a wavelength range of around 1520 to 1570 nm (see figure 3.5). This will show a range of whispering gallery modes with various radial and azimuthal mode numbers to which light is coupled. By adjusting the polarization of the incoming light, it is possible to couple only to TE or TM modes. When the proper modes are identified based on their free spectral range, they are measured with a fine scan, see inset of figure 3.5. This fine scan is subsequently saved onto the computer and processed further.

3.1.2. Production of tapered fibers

In order to couple laser light into the microdisks, tapered fibers are used. Tapered fibers are fibers with a small constriction in them, in this case of around 1-2 μm diameter. The small diameter of the tapered fiber allows evanescent coupling of the light in the fiber to an optical waveguide or cavity that is close by. The use

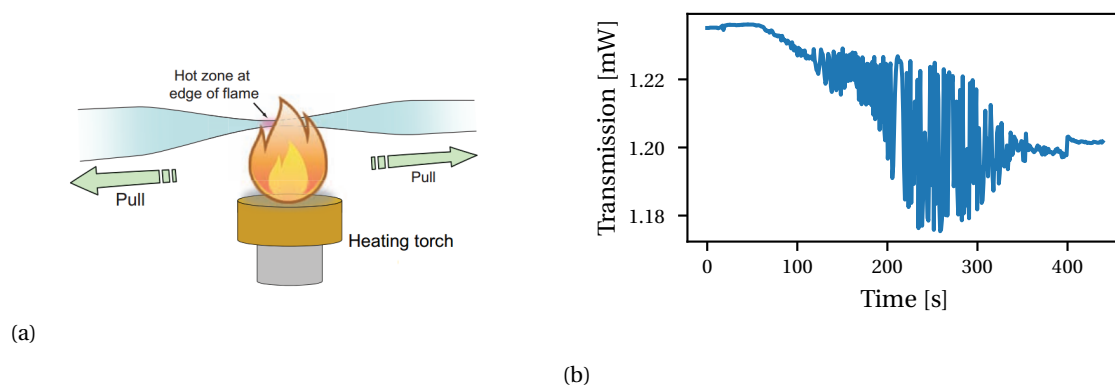


Figure 3.4: In figure 3.4a a schematic representation of the fiber tapering process is given [12]. In figure 3.4b the transmission through the fiber during the tapering process is shown. At around 400 seconds the fiber pulling process was stopped.

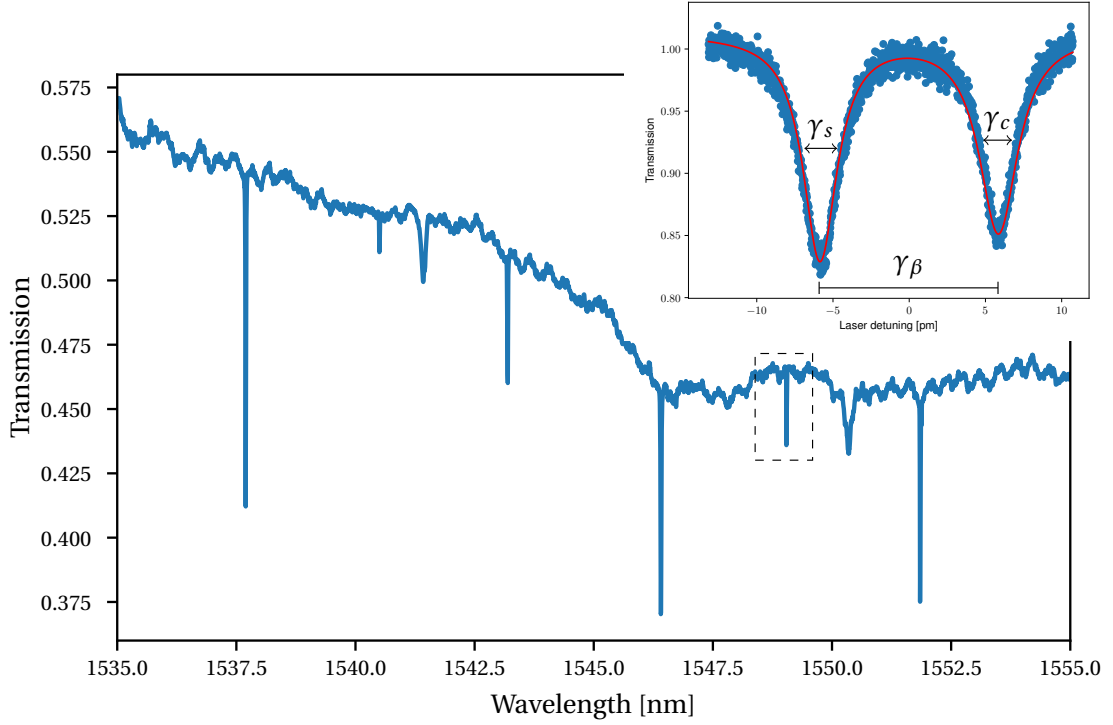


Figure 3.5: Coarse scan of a silicon microdisk with a $15\mu\text{m}$ radius and an inset of a fine scanned doublet resonance, indicated by the dashed rectangle. The parameters γ_s , γ_c and γ_β are the linewidths and the resonance splitting of the doublet resonance respectively.

of tapered fibers has been around since the 1980s and due to the high efficient coupling they provide and their maneuverability, tapered fibers have been widely used [30, 31]. In the past decades the production of tapered fibers has been studied and improved and since the end of the 1990s they have been used as a way to couple into whispering gallery mode resonators such as microspheres and -toroids [14, 32–34].

In order to make the tapered fibers for this thesis Corning SMF28e+ silica fiber with a core diameter of $8.2\mu\text{m}$ and a cladding diameter of $125\mu\text{m}$ is used. Before a piece of fiber is tapered two fiber connectors are spliced to each ends of the length of fiber. In the middle of the fiber a part of around 2 cm is stripped and cleaned with isopropyl alcohol. The fiber is then clamped to two Suruga Seiki stages with the stripped part of fiber suspended between the stages. A hydrogen torch with a HT-3 hush tip is positioned under the stripped part of the fiber by a Newport stage. The silica fiber is first molten by heating it. It is then tapered by moving the two Suruga Seiki stages outwards with a speed of $20\mu\text{m s}^{-1}$, pulling on the fiber until it is single-mode (see figure 3.4a). This process is monitored by sending in light at 1550 nm wavelength from a New Focus Vidia laser and analyzing the amplitude of the transmitted signal. When the fiber is being tapered the transmitted amplitude will show a number of oscillations and fluctuations. After the moment that the diameter falls below the single-mode cutoff diameter the fluctuations in the transmission will have seized and it will have returned to a stable signal (see figure 3.4b). In this configuration the fiber will only support the propagation of a single guided mode [31].

3.1.3. Radius-varying measurement method

The radius-varying measurement method separates between any losses induced by the bulk of the material and those of the surface effects. In order to do so, microdisks with a radius between $R = 5\mu\text{m}$ and $30\mu\text{m}$ in steps of $5\mu\text{m}$ are fabricated and measured [9]. The measurement process of the radius-varying method is consists of repeating the general measurement method for various resonances with radial mode $p = 1$ for all the disk sizes. By applying the proper analysis method to these measurements the bulk and surface effects can be effectively separated.

3.1.4. Power-varying measurement method

The goal of the power-varying measurement method is to derive the linear and non-linear absorption from the change in resonance wavelength and the change of the depth of the dip in transmission at resonance as a consequence of raised input powers [10]. By using the first variable optical attenuator, VOA 1, the input power to the microdisk is changed. To keep track of the power that is sent to the disk, a 90:10 beam splitter is placed just before the device and 10% of the power is redirected to a Thorlabs PM100D power meter. Increasing the power in the circuit will eventually cause the photodiode to react in a non-linear way or even saturation. To counteract this behavior a second VOA, VOA 2, is placed before the photodiode and its attenuation is adjusted with a PID algorithm such that the recorded signal is the same for the different levels of laser input power. The changes made to the basic setup to achieve this goal are indicated by a red shaded block in figure 3.1.

In order to provide consistency between uses of the measurement method, every step of the measurement routine is automated. The setup is controlled by a computer using a combination of scripts written in Python and LabVIEW.

VOA control

The laser power incident on the microdisk is determined by the amount attenuation VOA 1 provides. The intensity of the light that will be incident on the microdisk will be determined by the input parameters V_{start} , V_{diff} , and n , the number of steps in power the measurement routine should take. The first parameter V_{start} , is the initial voltage applied to VOA 1 and determines the starting power of the measurement method. The value is chosen such that the scanned resonance does not show any distortions. The second input parameter, V_{diff} , will determine the final voltage on VOA 1, $V_{\text{start}} - V_{\text{diff}}$, and with that the final power of the measurement routine.

To allow for a linear spacing between the measured powers, the VOA voltages are first converted to an amount of attenuation in decibels. Based on figure 3.6, the conversion equation between the VOA voltage and the amount of attenuation, $\text{Att} = 1.446 \cdot V^2$, is derived. These values for attenuation in decibels are then converted to factors of attenuations relative to the starting power. These steps are shown below where α indicates the attenuation factor:

$$\begin{aligned} \text{Att}_{\text{start}} &= 1.446 \cdot V_{\text{start}}^2 \text{ dB} & \rightarrow \alpha_{\text{start}} &= 1 \\ \text{Att}_{\text{end}} &= 1.446 \cdot (V_{\text{start}} - V_{\text{diff}})^2 \text{ dB} & \rightarrow \alpha_{\text{end}} &= 10^{(\text{Att}_{\text{start}} - \text{Att}_{\text{end}})/10}. \end{aligned}$$

The attenuation factors α_{start} and α_{end} are subsequently converted into a linearly spaced array $\tilde{\alpha}$ of length n . By applying some minor arithmetic this array is then translated back to the attenuation in decibels and an

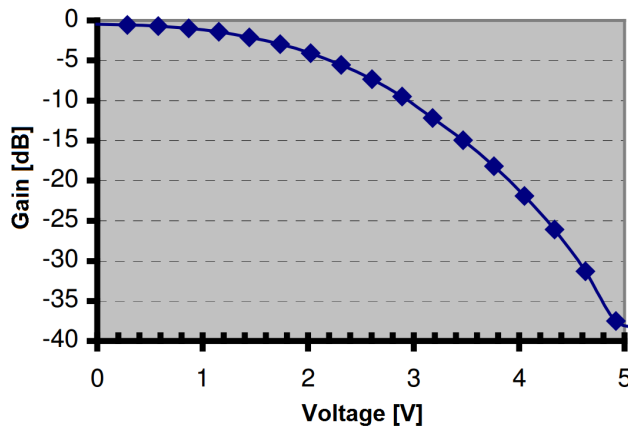


Figure 3.6: The relation between the applied voltage to the variable optical attenuator (VOA) and the attenuation it provides [28].

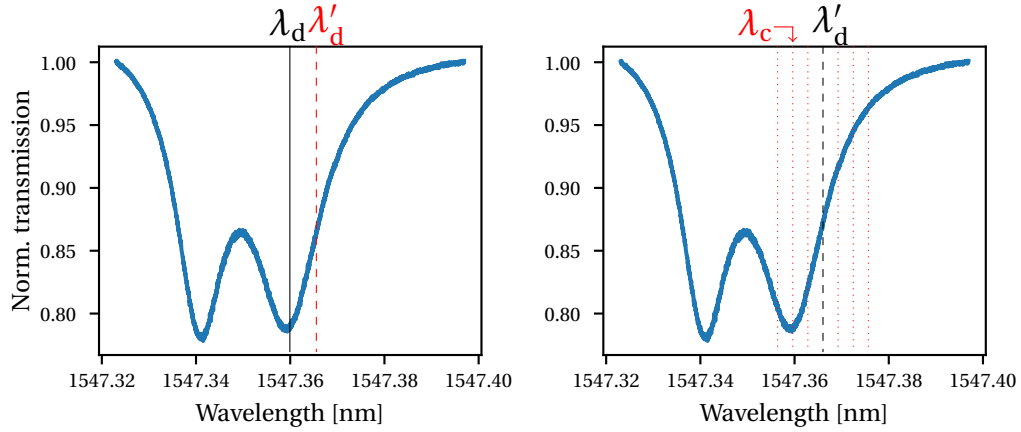


Figure 3.7: Schematic representation of the setup of the in-plane locking routine. In the left graph λ_d , black line, indicates the wavelength of the resonance dip as it was entered, and λ'_d , red dashed line, indicates the wavelength that is actually produced. In the right graph λ'_d is now indicated by a black dashed line and the red dotted line are the guessed resonances. The variable λ_c indicates the wavelength determined by voltage $V_{L,c}$.

array of VOA voltages

$$\begin{aligned}\bar{\alpha} &= [\alpha_{\text{start}}, \dots, \alpha_{\text{end}}] \\ \bar{\text{Att}} &= \text{Att}_{\text{start}} - 10\log_{10}(\bar{\alpha}) \\ \bar{V} &= \sqrt{\bar{\text{Att}}/1.446} = [V_1, \dots, V_n]\end{aligned}$$

which will produce an array of roughly linear spaced laser powers $\bar{P} = [P_1, \dots, P_n]$. During the power-varying measurement method the transmission spectrum is analyzed at every value of P_k in \bar{P} . To prohibit the scenario in which the photodiode displays non-linear behavior due to an increased laser amplitude, the amount of light is limited by VOA 2. The voltage that is supplied to this second VOA is determined iteratively with a PID controller. By applying $V_{L,bg} = 0.95\text{V}$ to the laser, the wavelength at the edge of the fine scan spectrum is probed. The transmission value at that wavelength is measured with input power P_1 at the beginning of the measurement routine of the power-varying measurement method; this value taken as the reference value T_{ref} . Before every measurement at an input power P_k , the transmission at the edge of the fine scan spectrum is compared to T_{ref} , and the voltage of VOA 2 is changed in order to match the two.

Position locking

For the power-varying measurement method it is important that the coupling depth of the resonance is consistent. Otherwise it will not be possible to extract an accurate value for the non-linear and linear absorption. To provide a consistent coupling, the position of the sample stage is adjusted using a PID algorithm in order to compensate for movements in the tapered fiber. This position correcting process will be called 'locking' in this thesis. Two types of locking are applied; Z-locking, where the sample is moved in the up or down direction, and in-plane locking, where the stage is moved towards or away from the tapered fiber in the x-y plane. Before a measurement at an increased laser amplitude, the input power is brought back to P_1 and the locking routine is performed to return the coupling to its original value.

If the fiber taper drifts downward and approaches the substrate, the overall level of the transmission will drop. This can probably be contributed to evanescent coupling to the substrate and the loss of light in this way. The Z-locking routine again applies $V_{L,bg}$ to the laser and compares the value of the transmission at that wavelength to the reference value T_{ref} . If this value is lower or higher the sample is moved in downward or upward direction respectively.

The in-plane locking works very similar to the Z-locking routine; the difference is that now the coupling of the resonance is compared to a reference value determined at the start of the measurement routine, and the position of the sample is adjusted to match the two. For the setup of the in-plane locking, the wavelength

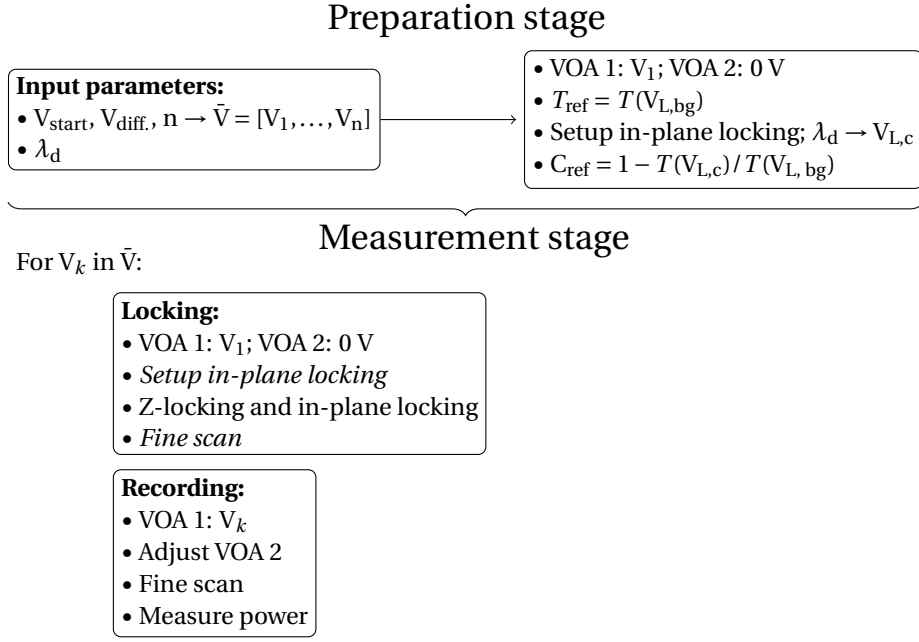


Figure 3.8: Schematic representation of the measurement process of the power-varying measurements. In a situation where an interleaved routine is not used, the steps written in italic in the Locking section can be disregarded.

of the resonance dip, λ_d , is entered at the start of the measurement routine (see figure 3.7). The laser input voltage corresponding to λ_d , $V_{L,d}$, is calculated by using the conversion factor between the input voltage V_L and the output wavelength of the laser that the Mach-Zehnder interferometer provides. Due to non-ideal behavior in the laser, $V_{L,d}$ will not produce the correct wavelength, but the laser will instead send out light with wavelength λ'_d . To find the correct voltage needed to reach λ_d , a range of voltages around $V_{L,d}$ are investigated. The voltage with the lowest transmission, $V_{L,c}$, is taken as the laser input voltage that will be used to probe the depth of the resonance dip and with that the value of the coupling. At the start of the measurement routine the reference coupling C_{ref} is determined according to the equation

$$C_{\text{ref}} = 1 - \frac{T(V_{L,c})}{T(V_{L,\text{bg}})}, \quad (3.1)$$

where the expression $T(V)$ indicates the transmission value at the wavelength produced by the laser input voltage V .

In the ideal case the position locking scheme will return the fiber to its original position. If, for example due to the stepping resolution of the stage, it is not possible to correct for the fiber movement with the desired precision, an 'interleaved' approach can be used. In this case an additional fine scan is made with input power P_1 at the end of the locking routine. The fine scan at P_k is then compared to the fine scan at P_1 at the end of the corresponding locking routine to analyze the difference in depth of the resonance dip and wavelength shift. The locking routine will then be used to correct for any major movements of the fiber.

If the microdisks are made out of a material with an refractive index comparable or less than that of the silica fiber, e.g. silicon nitride, the resonance wavelength of the microdisk can be influenced by the presence of the fiber. If the distance between the fiber and the microdisk varies, the resonance wavelength can change. In that case the interleaved approach is used to accurately determine $\Delta\lambda$. Because the resonance wavelength can change with a moving fiber, the in-plane locking setup has to be repeated with every repetition of the locking routine to determine the correct value for $V_{L,c}$.

Measurement routine

During the automated measurement routine, laser light at the powers P_k in the array \bar{P} are sent to the microdisk and the transmission spectrum is analyzed. These powers correspond to the array of VOA 1 voltages \bar{V} . The measurement routine can be separated into two stages; a preparation stage and the measurement

stage. A schematic overview of the measurement routine is shown in figure 3.8.

During the preparation stage, the input parameters are processed. After that the measurement stage begins, which consists of a locking routine and a recording routine. These two routines will be repeated for all powers in the array \bar{P} . During the locking routine the power is returned to P_1 and the position of the sample is adjusted for the fiber movement to keep the coupling constant. In the recording routine the power is increased to P_k , the VOA 2 voltage is properly adjusted and a fine scan of the resonance is taken. As the last step of the recording routine, the laser power is measured.

3.1.5. Stripped-oxide measurement method

As discussed in section 3.2, at the end of the fabrication of the silicon microdisks the material cleaned with a Piranha or an RCA clean. As a side-effect the silicon is oxidized and this oxide is subsequently stripped, removing a small layer of material. The thickness of the amount of the material can be accurately determined by analyzing the resonance spectrum of a microdisk before and after cleaning and stripping them.

The first step in the stripped-oxide measurement method is obtaining the resonance wavelength of one or more of the resonances of a silicon microdisk using the general measurement method. Secondly the sample is oxidized with the process that is in need of characterization and this oxide is then stripped. Due to this process the microdisk resonances will have shifted to the blue sided of the spectrum. The shifted versions of the resonances that were measured before the oxidation process are measured again and their resonance wavelength is determined. Using a conversion factor obtained from simulations with COMSOL Multiphysics [17] (see section 2.5.1), the resonance wavelength shift can be converted into a thickness of stripped material.

To make sure that the resonance wavelength shift is measured correctly a High Finesse WS6 wave meter is used. A 99:1 beam splitter is used to redirect 1% to this device. The added beam splitter and the wave meter are indicated in figure 3.1 surrounded by a gray box.

3.2. Fabrication of the samples

To test the measurement methods described in this thesis, two materials are investigated; silicon and silicon nitride, Si_3N_4 . The silicon comes in the form of a layer of 250 nm silicon on top of a $3\text{ }\mu\text{m}$ SiO_2 substrate. The silicon nitride has a thickness of 350 nm and has a silicon substrate. Both materials share the same fabrication processes, but different chemicals were used as etching and cleaning agents for each material [4]. The fabricated samples were provided by the daily supervisor, Andreas Wallucks.

Starting from commercial silicon-on-insulator or silicon nitride-on-silicon wafers, the microdisk structures are defined by using electron-beam (E-beam) lithography and a positive E-beam resist. The designs used in this thesis, shown in figure 3.9b, were drawn in AutoCAD and subsequently prepared for use in the E-beam lithography machine with GenISys BEAMER. In AutoCAD the areas which should be exposed with the E-beam are defined and with GenISys BEAMER these areas are divided into small trapezoids that will be exposed for a

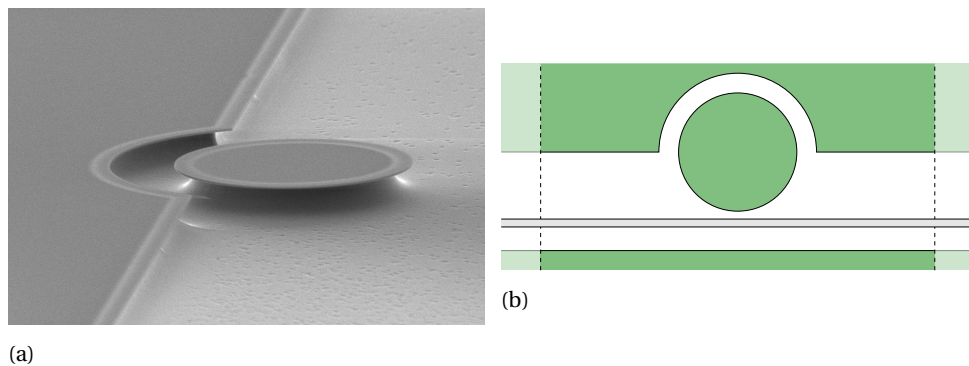


Figure 3.9: Figure 3.9a shows a scanning electron microscope image of an undercut microdisk. Figure 3.9b shows a schematic representation of design of the samples. The samples are diced at the dashed lines, leaving them to be $640\text{ }\mu\text{m}$ wide. The fiber trenches have a width of $50\text{ }\mu\text{m}$. The gap between the microdisk and the rest of the material is around $4\text{ }\mu\text{m}$. The image is not to scale.

certain amount of time. The pattern of these trapezoids are dependent on a number of parameters, such as the base size and the distribution of these trapezoids. As an initial test settings previously used in the fabrication of nanobeam resonators were applied to the microdisk design. This set of parameter values is called the 'standard' dosing pattern. Using the radius-varying measurement method, a set of silicon microdisks made with the standard lithography settings is compared to a set of silicon microdisks made a different dosing pattern. This set of lithography settings is designed to reduce the surface roughness on the edge of the microdisk and is called the 'trial' dosing pattern. The samples for the measurement methods besides the radius-varying method were made with the trial lithography settings.

After the resist is exposed by the E-beam radiation, it is developed and the defined structures are translated onto the silicon or silicon nitride layer by using an inductively coupled reactive-ion etch. For the silicon disks SF_6 gas is used as an etchant and for silicon nitride CHF_3 . During the etching of the chips with the silicon microdisks O_2 gas is supplied as sidewall passivation.

To allow for easy access to the disks with a tapered fiber the samples are diced. After this step the photoresist is dissolved, removed and the sample is cleaned with an organic solvent. The devices are subsequently cleaned more thoroughly with a Piranha solution or subjected to an RCA clean [11]. This process will additionally reduce the sidewall roughness of the disks.

The silicon microdisks are undercut by etching the silicon oxide with a 40% solution of hydrofluoric acid (HF). After the undercut the silicon disks are cleaned with an RCA cleaning mixture. This oxidizes the silicon and this oxide is subsequently stripped using a 4% HF solution. To investigate the oxidation of a number of fabrication processes, this step of oxidizing the microdisks and stripping the material was repeated with a Piranha solution, an RCA-1 clean and an RCA-2 clean for the stripped-oxide measurement method. The chips with the silicon nitride disks were undercut with a wet etching procedure using KOH. This undercutting process was finished with a cleaning step with a Piranha solution.

To prevent moisture contamination of the samples, they are stored in a nitrogen purged desiccator after fabrication.

3.3. Analysis

After the measurements are done, the data that has been gathered first has to be properly analyzed before any information can be extracted.

3.3.1. General analysis

After scanning a resonance a doublet Lorentzian, equation 2.2, is fitted to the data to derive the linewidths, γ_c and γ_s , the mode splitting γ_β , the resonance frequency ω_0 and the external decay rate γ_{ext} . The external decay rates are subtracted from the linewidths to calculate the intrinsic optical losses, $\gamma_{c,i}$ and $\gamma_{s,i}$. The fitted parameter values are subsequently converted to the Q factors, $Q_{c,i}$, $Q_{s,i}$ and Q_β .

3.3.2. Analysis of the radius-varying measurement method

After the radius-varying measurement method is completed, the scanned resonances are fitted and two intrinsic Q factors and one value of Q_β will have been obtained for every doublet resonance measured. The first step in the analysis is to fit equation 2.12 for Q_β to the measured values to extract the value of the surface roughness parameter $\sqrt{L_c}\sigma_r$. With this parameter the surface scattering Q factor Q_{ss} can be calculated using equation 2.9. These calculated values are subtracted from the values of $Q_{\{c,s\},i}$. To the remaining Q factor the sum of Q_{sa} , equation 2.15, and the constant Q_{bulk} are fitted. From this fitting procedure the unknown values of the surface absorption parameter $\gamma_{\text{sa}}\zeta$ and Q_{bulk} are obtained [9].

3.3.3. Analysis of the power-varying measurement method

When the measurements are done with the power-varying measurement method, one ends up with a number of fine scanned resonances at different laser powers P_1 through P_n . If the interleaved approach was used, all the fine scanned resonances will also have a corresponding low power fine scan taken at P_1 . A doublet Lorentzian is fitted to all the fine scans taken at P_1 and the values for γ_c , γ_{ext} and γ_β are extracted. Of all fine scanned resonances the value of T_{min} and the resonance wavelength are manually determined.

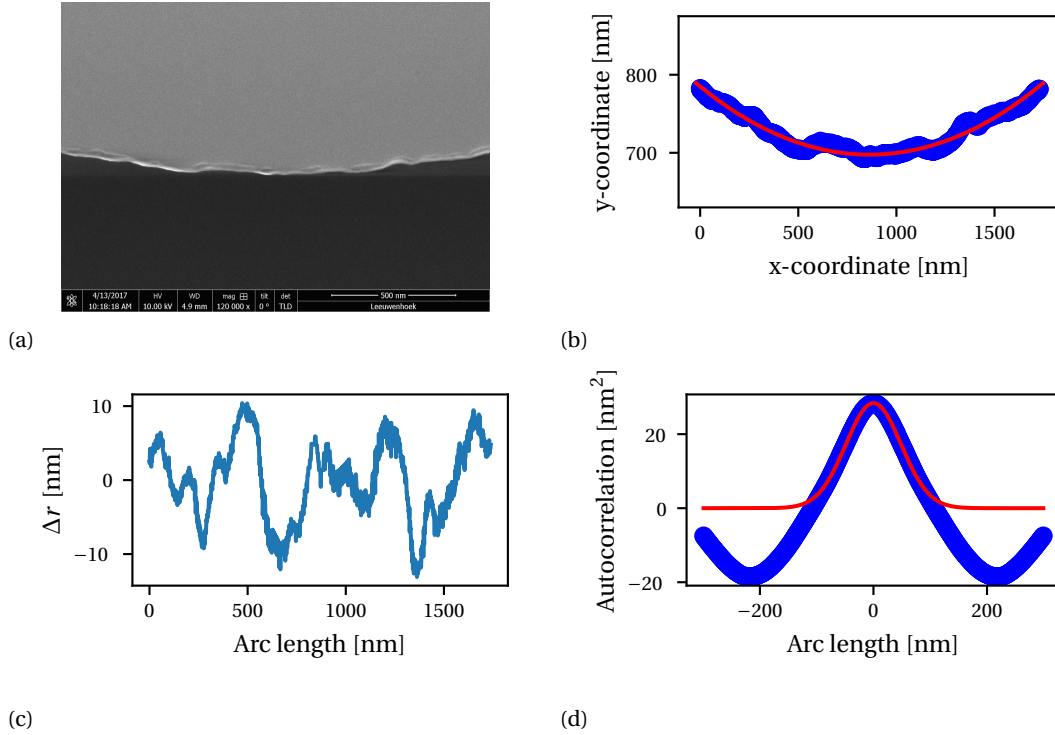


Figure 3.10: Figure 3.10a shows the image of a silicon microdisk with $R = 5\mu\text{m}$ fabricated with the standard E-beam dosing pattern. Figure 3.10b shows the disk edge converted into a set of points in blue with the corresponding fit in red. In figure 3.10c the distance of the points to the fit, Δr , can be seen as a function of the arc length of the disk edge; figure 3.10d shows an excerpt of the autocorrelation of Δr in blue and a Gaussian fit to the center bump in red.

With the value of T_{\min} of the measurement at P_k and the fitting parameters γ_c , γ_{ext} and γ_β from the fine scan at P_1 , the normalized non-linear absorption γ'_{nla} can be calculated with equation 2.33. In the scenario that the interleaved approach is used the fitting parameter values from the cold cavity fine scan that corresponds to the measurement at laser power P_k are used. From the measured input power P_i , the values of T_{\min} and the calculated values of γ'_{nla} , the dropped power $P_d = (1 - T_{\min})P_i$ and the internal cavity energy $U_c = P_d/\gamma_t = P_d/(\gamma_{\text{cold}}(1 + \gamma'_{\text{nla}}))$ are calculated. The total linewidth of the cold cavity is given by $\gamma_{\text{cold}} = \gamma_c + \gamma_{\text{ext}}$ [10].

The difference between the resonance wavelength at P_k and P_0 is defined as the resonance wavelength shift $\Delta\lambda$. To obtain the value of the normalized linear absorption γ'_{la} , equation 2.36 is fitted to the slope of the measured values of resonance wavelength shift $\Delta\lambda/P_d$ with the dropped power P_d and the normalized non-linear absorption γ'_{nla} as independent variables [10].

3.3.4. Analysis of the stripped-oxide measurement method

After the measurements of the microdisks before and after applying the oxidizing fabrication procedure are done, a doublet Lorentzian is fitted to both two groups of fine scanned resonances. These fits will return the resonance wavelengths of the two groups. After the fitting step the difference between the resonance wavelengths of the microdisks before oxidizing and their shifted counterparts is calculated. This wavelength difference will subsequently be converted to the thickness of the stripped oxidized material with the use of the conversion factor as derived in section 2.5.1.

3.3.5. Image analysis

In order to corroborate the data for the value of the surface roughness parameter $\sqrt{L_c}\sigma_r$ derived from the radius-varying measurement method the scanning electron microscope (SEM) images are analyzed [12]. The first step in the analysis process is to convert the SEM image (see figure 3.10a), from a gray scale to a black and white image. Per column of the image, the position of the disk edge is determined based on where the images

changes from black to white. These points are shown in blue in figure 3.10b. In this graph the bottom left of the SEM image corresponds to an x- and y-coordinate of 0 nm. After that step a circle is fitted through these points, shown as the red curve in 3.10b. To identify the roughness of the disk edge, the distance between the fitted circle and the points, Δr , is calculated. These distances are then plotted against the arc length of the circle as show in figure 3.10c. From this data an autocorrelation is determined. The fit of a Gaussian distribution to the center peak of this autocorrelation then reveals the values of L_c and σ_r . The autocorrelation and the Gaussian fit can be seen in figure 3.10d.

3.3.6. Uncertainty calculation

When implementing a measurement method, the uncertainty in that method should also be considered. During the characterization of a material or fabrication process, uncertainty in the obtained values arises from the measured quantities, during the fitting of parameters and from the analysis of the data. When multiple measured quantities are used in the same equation, they are assumed to be independent for the calculation of the propagated uncertainty. With measured quantities $a \pm \Delta a, b \pm \Delta b, \dots$ the uncertainty of equation $f(a, b, \dots)$ is given by [35]

$$\Delta f = \sqrt{\left| \frac{\partial f}{\partial a} \right|^2 |\Delta a|^2 + \left| \frac{\partial f}{\partial b} \right|^2 |\Delta b|^2 + \dots} \quad (3.2)$$

In the fitting routines used in the analysis of the measurements, uncertainties in the dependent variables are incorporated. In situations where uncertainties in the independent variables are significant, orthogonal distance regression is used to also take these values into consideration [36].

4.1. Radius-varying measurement method

In this section the results of the radius-varying measurement method are presented and discussed. The initial intent was to follow implement the method as described in reference [9] in which the resonant TM modes of the microdisks were measured. During the testing of this setup it became clear that it was not possible to measure the TM modes of the microdisks with a high radius. The transmission dips of these resonators were very broad and showed a lot of overlap, prohibiting proper measurement of the doublet Lorentzians. This in contrast to the TE modes as can be seen in figure 4.1. The measurements in this thesis were therefore performed by measuring the TE modes of the microdisks and the supporting theory has been extended for this use (see section 2.3.3). Due to the fact that this behavior is not seen in smaller microdisks, an explanation is suggested that this behavior is the result of damaging or contamination by dirt from the dicing process. This dirt would have a larger impact on the larger disks because they have a larger surface. The electric field associated with the TM modes is larger at the top and bottom of the disks than the electric field for the TE modes at the same position (see figure 2.3), therefore the TM modes could be more sensitive to damage in those places than the TE modes.

The results of the radius-varying measurement method presented here are from measurements done on two sets of silicon microdisks on a silicon-on-insulator chip. The lithography step of one of the two sets was performed the standard E-beam lithography settings, while the other set was made with the trial dosing pattern, as described in 3.2. The hypothesis is that the microdisks made with the trial set of parameter values will have less surface roughness than the microdisk set made with the standard lithography settings due higher accuracy in the exposure of the resist.

The value for the surface roughness parameter $\sqrt{L_c}\sigma_r$ was derived from the measurement and fit of Q_β . The

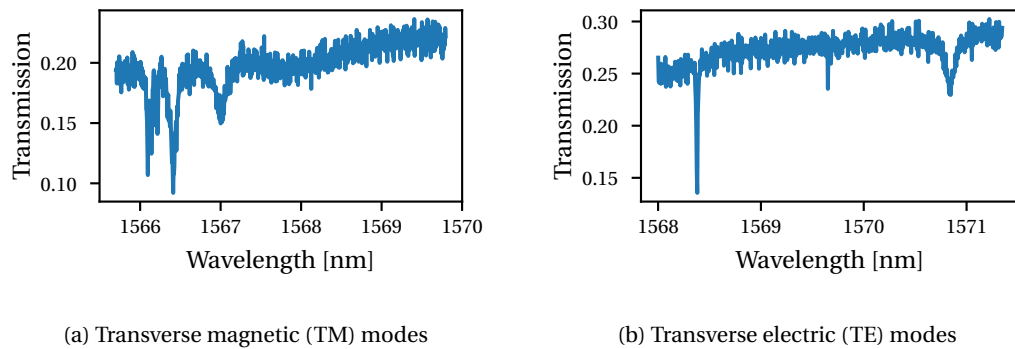


Figure 4.1: Excerpt of the course scan of a silicon microdisk with a radius of $R = 25 \mu\text{m}$. One can see that the transmission dips of the TM modes in the graph on the left have much overlap; the resonances of the TE modes on the right show a larger spacing.

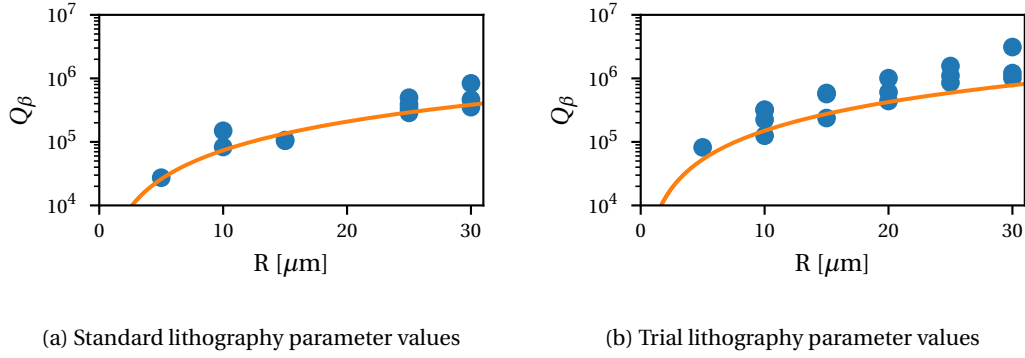


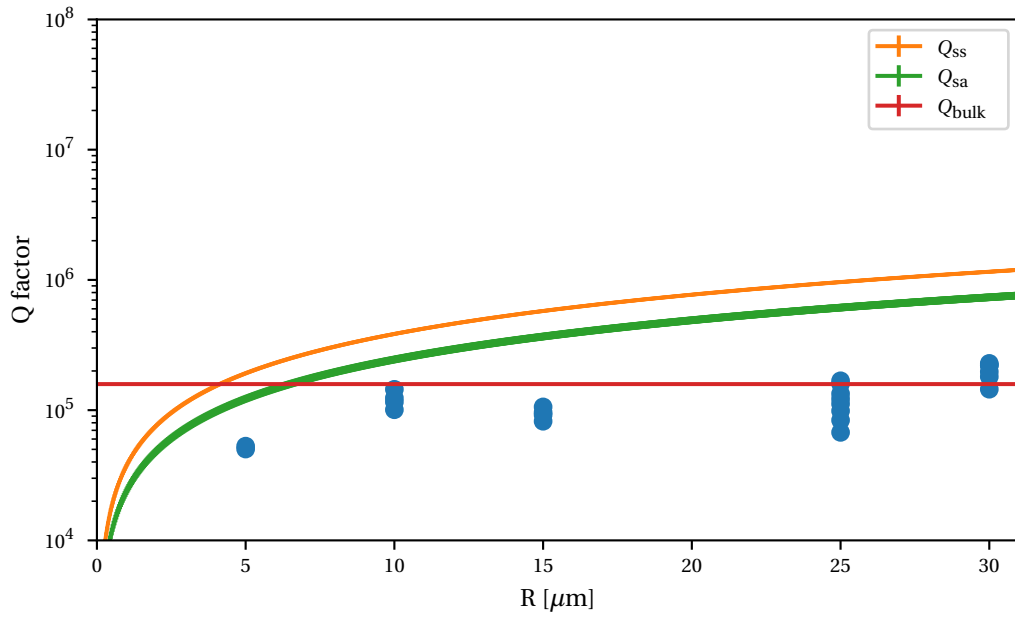
Figure 4.2: Plots of the measurements of Q_β and the fit according to equation 2.12.

values and the fit can be seen in figure 4.2. Due to difficulties of obtaining a proper fit of the measured resonances for the silicon microdisks with the standard lithography dosing pattern, there was no measurement point for the $25\mu\text{m}$ radius disk. For the silicon microdisks with the standard lithography settings a value for $\sqrt{L_c}\sigma_r$ of $4.266 \pm 0.007\text{ nm}^{3/2}$ is found; for the microdisks made with the trial dosing pattern the value is $2.096 \pm 0.0016\text{ nm}^{3/2}$. From these numbers it can be seen that the trial E-beam lithography settings improve the surface roughness with a factor of two. The same qualitative improvement can be seen in the results of the image analysis, shown in table 4.1. There is however a difference of an order of magnitude between the values for $\sqrt{L_c}\sigma_r$ for the image analysis and the radius-varying measurement method. An explanation could be that the roughness felt by the resonant modes in the microdisk is less than the actual profile on the edge of the disk.

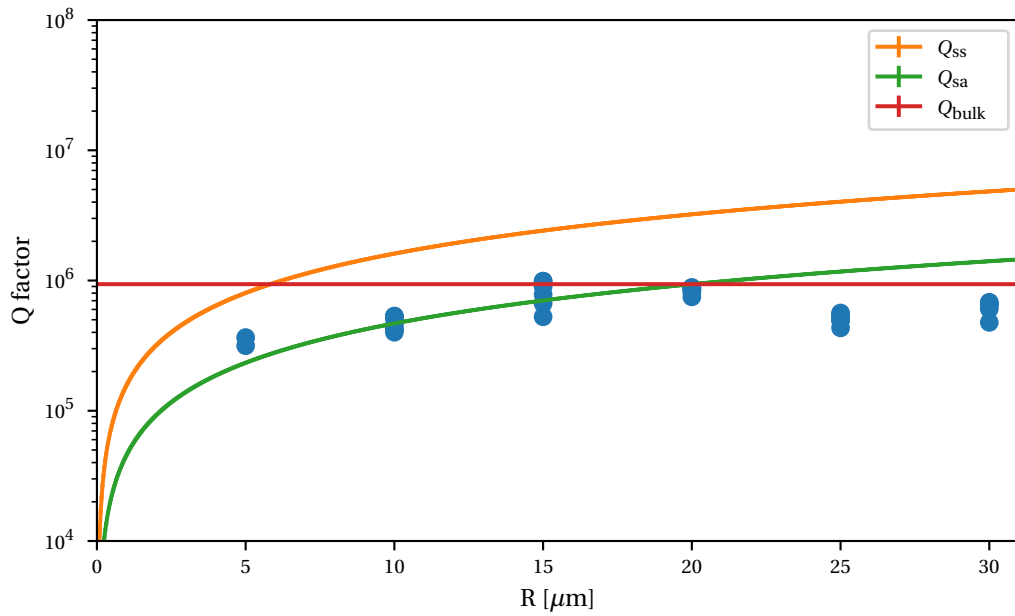
After performing the remaining part of the radius-varying measurement method the results for Q_{ss} , Q_{sa} , Q_{bulk} and the measured values for the intrinsic Q factor are shown in figure 4.3. Values for the surface roughness parameter $\sqrt{L_c}\sigma_r$, the surface absorption parameter $\gamma_{sa}\zeta$ and the bulk absorption Q factor Q_{bulk} can be seen in table 4.2. A plot of the corresponding Q factors, Q_{ss} , Q_{sa} and Q_{bulk} can be seen in figure 4.3. Following from the values of $\sqrt{L_c}\sigma_r$ obtained from the measurements of Q_β , this figure shows a value for Q_{ss} for the trial set of lithography parameter values which is a factor of four larger than for the disks made with the standard set. A peculiar part of these measurements is the fact that the values for Q_{bulk} differ by roughly a factor of six. The two sets of microdisks were fabricated on the same silicon-on-insulator sample and should not show a difference in bulk absorption. The cause of this discrepancy can probably be traced back to the low signal to noise ratio of the input data due to the lack of amplification. This can lead to errors in determining the internal linewidths of the transmission dips and ultimately to a value for the bulk and surface absorption different from reality. After these measurements were concluded, an amplifier was added to the experimental setup but the measurements have not been repeated. In any future measurements it is also advised to use more data points, perhaps from different sets of microdisks with the same fabrication procedure on the same sample, to improve the performance of the fitting algorithm. In figure 4.3 and table 4.2 it can be seen also be seen that there is a difference in Q_{sa} or $\gamma_{sa}\zeta$ but due to the fact that this variable is obtained from the same fitting step as the one from which Q_{bulk} is derived, it is not advised to draw conclusions about the surface absorption from this measurement.

	Standard	Trial
σ_r	$5.328 \pm 0.006\text{ nm}$	$2.817 \pm 0.007\text{ nm}$
L_c	$68.98 \pm 0.18\text{ nm}$	$78.0 \pm 0.5\text{ nm}$
$\sqrt{L_c}\sigma_r$	$44.25 \pm 0.05\text{ nm}^{3/2}$	$24.89 \pm 0.07\text{ nm}^{3/2}$

Table 4.1: Values for the correlation length L_c and amplitude σ_r of the Gaussian distribution of surface roughness, and the surface roughness parameter $\sqrt{L_c}\sigma_r$ derived from the image analysis for a microdisk with $R = 5\mu\text{m}$. The data is shown for silicon microdisks made with the standard and the trial set of lithography parameter values.



(a) Standard lithography parameter values



(b) Trial lithography parameter values

Figure 4.3: Plots of the measurements of the internal Q factors and the resulting functions for the surface scattering Q factor Q_{ss} , the surface absorption Q factor Q_{sa} and the absorption Q factor Q_{bulk} from the radius-varying measurement method.

Table 4.2: Results of the radius-varying measurement method comparing silicon microdisks made with the standard and trial set of parameter values for E-beam lithography. The parameters $\sqrt{L_c}\sigma_r$ and $\gamma_{sa}\zeta$ are known as the surface roughness and surface absorption parameters in the context of this thesis and Q_{bulk} is the Q factor for the bulk absorption.

	Standard	Trial
$\sqrt{L_c}\sigma_r$	$4.266 \pm 0.007 \text{ nm}^{3/2}$	$2.096 \pm 0.0016 \text{ nm}^{3/2}$
$\gamma_{sa}\zeta$	$(7.5 \pm 0.5) \times 10^4 \text{ rad/s} \cdot \text{m}$	$(3.88 \pm 0.06) \times 10^4 \text{ rad/s} \cdot \text{m}$
Q_{bulk}	$(1.585 \pm 0.008) \times 10^5$	$(9.38 \pm 0.05) \times 10^5$

4.2. Power-varying measurement method

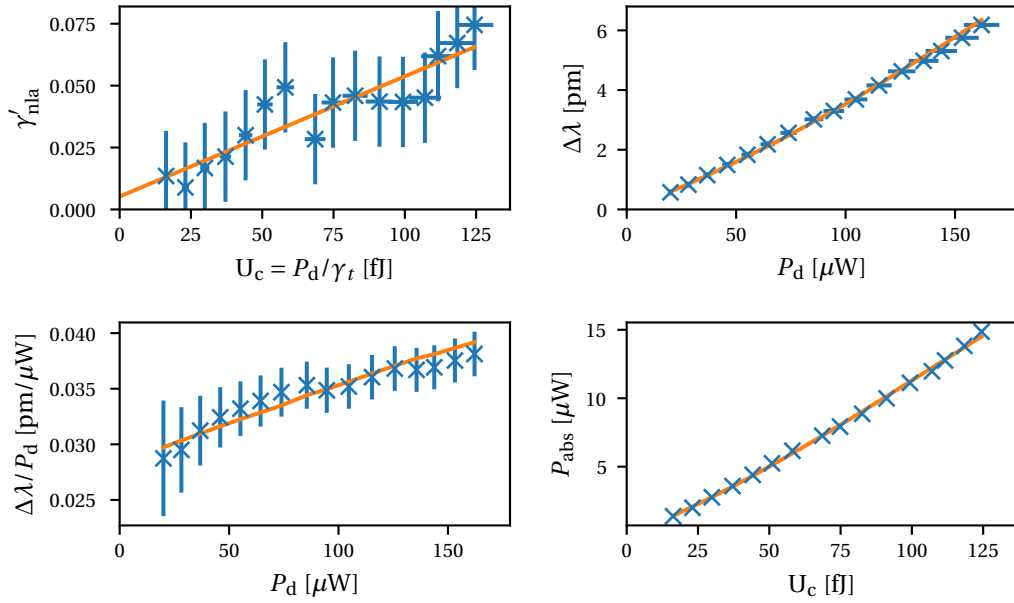


Figure 4.4: Results from the power-varying measurement method for a silicon microdisks with a radius of $15 \mu\text{m}$. Top left: The normalized non-linear absorption γ'_{nla} as a function of the internal cavity energy U_c and fit. Top right and bottom left: The resonance wavelength shift $\Delta\lambda$ as a function of dropped power P_d , and the slope of this function with a fit. Bottom right: Absorbed power P_{abs} as a function of U_c as explained in section 2.4.1.

In this section the results of the power-varying measurement method are presented. This method was applied to a silicon microdisk with a radius of $15 \mu\text{m}$ and a $10 \mu\text{m}$ radius silicon nitride microdisk. The fabrication process of these samples can be read in section 3.2.

The analysis of the power-varying measurement method was performed on a single execution of the measurement routine for the silicon microdisks, while for the silicon nitride the measurement was repeated three times and the data of these three measurements were combined. The measurements on the silicon nitride were performed with the interleaved approach, as explained in section 3.1.4, while for the silicon microdisks this was not the case. The results of the cold cavity fit can be seen in table 4.3.

The first step in the power-varying measurement method is deriving the non-linear absorption from depth of the transmission dip. The results of this step can be seen in the top left corner of figure 4.4 and figure 4.5 for the silicon and silicon nitride disks respectively. The non-linear absorption of the silicon microdisks shows a linear dependence on the internal cavity energy U_c due to two-photon absorption in the range of input powers with a maximum of $750 \mu\text{W}$ that was used [10]. The deviations from a linear functions are probably due to movement of the tapered fiber and a limited resolution of the locking setup. Using a fixed waveguide to couple light into the microdisk would probably resolve this problem.

Table 4.3: Results of the fit of the cold cavity resonance used in the power-varying measurement method; $\gamma_{c,i}$ and $\gamma_{s,i}$ are the internal loss rates, γ_{ext} is the external linewidth and γ_{β} is the doublet mode splitting.

	Silicon	Silicon nitride
λ	1540.48 nm	1547.38 nm
$\gamma_{c,i}$	170 ± 3 MHz	1.82 ± 0.04 GHz
$\gamma_{s,i}$	187 ± 3 MHz	1.64 ± 0.03 GHz
γ_{β}	730 ± 2 MHz	2.66 ± 0.02 GHz
γ_{ext}	23.4 ± 0.3 MHz	174 ± 0.03 MHz

As a consequence of limitations to the experimental setup at the time at which the measurements of the silicon nitride were performed, the input power used in these measurements was not larger than $27.5 \mu\text{W}$. The silicon nitride disks also show a larger linewidth than the silicon microdisks, which causes a lower internal cavity energy. The constant value for γ'_{nla} as a function of U_c is therefore as expected at these low values of the internal cavity energy. The fluctuations in this measurements could again be solved by using a fixed waveguide.

One of the points that should be fixed in any future iterations of this method is the fact that the non-linear absorption is not zero at zero internal cavity energy. This probably is related to a potential discrepancy between the fit and the data of the cold cavity spectrum. The non-linear absorption is calculated based on the parameters determined by the fit of the doublet Lorentzian to the cold cavity spectrum and the value of T_{min} that is determined manually. When the value of T_{min} of the measured cold cavity spectrum is different from the value of T_{min} of the fitted Lorentzian, then γ'_{nla} will have an offset. Improvements can be sought in the application of better fitting algorithms, as for example shown in reference [37], in an improved approach to subtract background signals or in different ways to determine the values of T_{min} and the resonance wavelength.

In the top right and bottom left of figures 4.4 and 4.5 one can see the resonance wavelength shift $\Delta\lambda$ as a function of dropped power P_d , and the slope of this measurement respectively. It can be seen that the graph

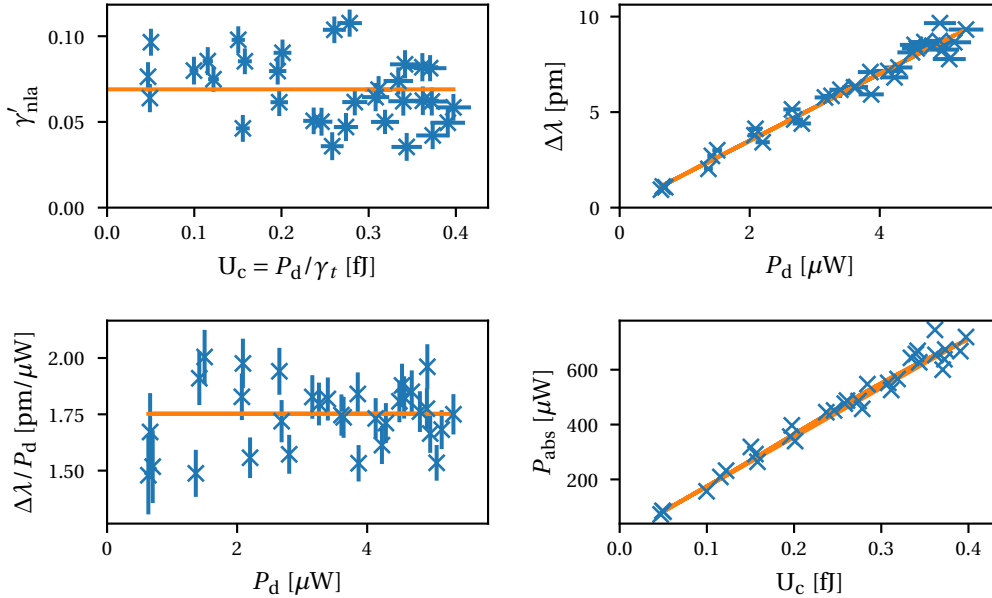


Figure 4.5: Results from the power-varying measurement method for the silicon nitride microdisks. Top left: The normalized non-linear absorption γ'_{nla} as a function of the internal cavity energy U_c and fit. Top right and the bottom left: The resonance wavelength shift $\Delta\lambda$ as a function of dropped power P_d , and the slope of this function with a fit. Bottom right: Absorbed power P_{abs} as a function of U_c as explained in section 2.4.1; this graph shows P_{abs} to be larger than the dropped power P_d and is therefore erroneous.

for $\Delta\lambda$ for the silicon microdisk is not a linear function; this is due to the non-constant non-linear absorption that this material exhibits. The silicon nitride disk does show a linear relation between $\Delta\lambda$ and P_d due to the constant non-linear absorption.

Using the fitted function from the non-linear absorption, the slope of equation 2.36 can be fitted to the slope of the measured resonance wavelength shift. In this way a value for the normalized linear absorption γ'_{la} and the factor C can be obtained. For the silicon microdisk the result is $\gamma'_{la} = 0.12 \pm 0.01$ and $C = (2.20 \pm 0.15) \times 10^5$ pm/W. Using the value for the parameter $\sqrt{L_c}\sigma_r$ from the radius-varying measurement method, it can be calculated that the scattering loss rate of the silicon microdisk is $\gamma_{ss} = 88$ MHz. From the assumption that the cold cavity linewidth is only comprised of linear absorption losses or scattering losses, the value of γ'_{la} arising from the measurement with the radius-varying measurement method is found to be $\gamma'_{la} = 0.57$, which is equal to a value found in literature for a silicon microdisk with a $10\mu\text{m}$ radius [10]. This does unfortunately not match the value measured with the power-varying measurement method.

If a material shows a non-linear absorption that is a constant function of U_c and therefore P_d , there will be multiple possible values of γ'_{la} and C that will result in a fit to the data, and this method will result in an ambiguous and unusable result. Therefore no values for γ'_{la} and C are given for the silicon nitride disk.

A different way to calculate γ'_{la} is to calculate a value of C , C_{calc} , and using this to convert $\Delta\lambda$ to the absorbed power P_{abs} and fitting an expression for P_{abs} as a function of U_c to this data (see section 2.4.1). These graphs are shown in the bottom right corner of 4.4 and 4.5. The value for C_{calc} for the silicon microdisk is $(4.1 \pm 0.3) \times 10^5$ pm/W with a corresponding value of $\gamma'_{la} = 0.066 \pm 0.002$. These values differ with a factor of two from the measured values from the power-varying measurement method. As shown in figure 4.5, the calculated values of the absorbed power for the silicon nitride are much larger than the input power; this is obviously incorrect. A possibility why this method is not applicable on this sample is due to the lack of thermal isolation due to the use of silicon as the material for the pedestal [9].

Table 4.4: Parameters used to calculate coefficient C for silicon microdisk on a SiO_2 pedestal and a silicon nitride disk on a silicon pedestal. The values for r_{max} and r_{min} are estimated based on microscope images of the sample.

	Silicon	Silicon nitride
$\frac{dn}{dT}$	$(1.86 \pm 0.08) \times 10^{-4} \text{ K}^{-1}$ [38]	$(2.45 \pm 0.09) \times 10^{-5} \text{ K}^{-1}$ [39]
n_d	3.48 [40]	1.996 [41]
κ	$1.4 \pm 5\% \text{ W m}^{-1} \text{ K}$ [42]	$148 \pm 5.8\% \text{ W m}^{-1} \text{ K}$ [42]
h_{ped}	$3\mu\text{m}$	$5\mu\text{m}$
R	$15\mu\text{m}$	$10\mu\text{m}$
r_{min}	$11.7\mu\text{m}$	$4.8\mu\text{m}$
r_{max}	$12.2\mu\text{m}$	$7.2\mu\text{m}$

4.3. Stripped-oxide measurement method

The oxidation of silicon by three fabrication methods was investigated as described in section 3.1.5;

- Piranha clean at 90°C for 10 minutes,
- RCA-1 clean at 75°C for 10 minutes [11],
- RCA-2 clean at 75°C for 10 minutes [11].

After applying these cleaning procedures any oxidized silicon was stripped with a 4 % HF solution. The fabrication methods were applied in the order mentioned above on a silicon-on-insulator sample. Three different microdisk resonators with a radius of $5\mu\text{m}$ were used for the measurements. The microdisks had spent several days in a nitrogen purged desiccator prior to the measurements, so it is assumed that a native oxide of an estimated 0.19 ± 0.01 nm thickness was built up on the silicon surface [43]. Before the microdisks underwent the fabrication methods, this oxide was stripped by dipping it in a dilute HF solution. This stripped oxide and the silicon dioxide stripped by the fabrication processes is taken into account when converting $\Delta\lambda$ to Δ_{ox} as described in section 2.5.1.

Table 4.5: Table of the results of the stripped-oxide measurement method. Columns noted λ_1 and λ_2 are the resonance wavelengths of the microdisk before and after applying the fabrication process and the HF dip. $\Delta\lambda$ and Δ_{ox} indicate the resonance wavelength shift and the thickness of the stripped oxidized silicon.

Process	λ_1 [nm]	λ_2 [nm]	$\Delta\lambda$ [nm]	Δ_{ox} [nm]
Piranha	1542.79	1538.12	$4.67 \pm 4 \times 10^{-5}$	1.7 ± 0.6
	1542.07	1538.09	$3.98 \pm 3 \times 10^{-5}$	1.5 ± 0.6
	1540.71	1537.66	$3.05 \pm 3 \times 10^{-5}$	1.1 ± 0.6
			$3.90 \pm 2 \times 10^{-5}$	1.4 ± 0.3
RCA-1	1563.57	1556.26	$7.30 \pm 6 \times 10^{-5}$	2.5 ± 0.7
	1562.02	1556.10	$5.91 \pm 6 \times 10^{-5}$	2.1 ± 0.7
			$6.61 \pm 4 \times 10^{-5}$	2.3 ± 0.5
RCA-2	1556.26	1554.08	$2.18 \pm 1 \times 10^{-4}$	0.75 ± 0.8
	1562.34	1560.13	$2.21 \pm 4 \times 10^{-4}$	0.76 ± 0.8
	1536.14	1534.06	$2.08 \pm 3 \times 10^{-4}$	0.74 ± 0.8
	1562.45	1560.29	$2.16 \pm 3 \times 10^{-2}$	0.75 ± 0.8
	1556.10	1553.93	$2.17 \pm 9 \times 10^{-5}$	0.75 ± 0.8
			$2.16 \pm 6 \times 10^{-3}$	0.75 ± 0.4

The results of the measurements can be seen in table 4.5. The resonance wavelengths before and after applying the fabrication process and the HF dip are shown in the second and third column respectively. In the fourth and fifth column one can find the resonance wavelength shift $\Delta\lambda$ and the corresponding thickness of the stripped oxidized material Δ_{ox} . In the last row of every block dedicated to a certain fabrication process, average values are given for $\Delta\lambda$ and Δ_{ox} . The qualitative comparison of the average values of Δ_{ox} for the different processes correspond to the experiences from other lab members. The values of the material removed due to the RCA clean correspond to the values between 2 and 8 nm reported in literature [44–46].

5

Conclusion

During the research for this thesis the groundwork has been laid for three measurement methods which use microdisk cavities; the radius-varying, the power-varying and the stripped-oxide measurement method.

Radius-varying measurement method

For the radius-varying measurement method, based on previous work done by Borselli et al. [9], the theory is extended to allow the use of TE modes to characterize the surface scattering, surface absorption and bulk absorption of materials and fabrication processes. In the measurements done with this method, it was successful to measure a qualitative difference in surface roughness between two sets of silicon microdisks. They were fabricated using two sets of parameter values, named the 'standard' and the 'trial' set, for the distribution of the dosing pattern of the electron-beam lithography exposure. It was found that the value for the surface roughness parameter $\sqrt{L_c}\sigma_r$ for the trial set of lithography parameter values was a factor of two smaller than the one found for the standard set. This was also corroborated by analysis of scanning electron microscope images of the microdisks. The fitting routine that determines the values for surface and bulk absorption produced erroneous results. The suggestion is that this error will be fixed by increasing the signal to noise ratio of the measurements and increasing the number of measured resonances.

Power-varying measurement method

The implementation of the power-varying measurement was based on a different publication by Borselli et al. [10]. With this method it is possible to determine the non-linear and the linear absorption of a microdisk by analyzing the change in the depth of the transmission dip at resonance and the shift of the resonance wavelength as a function of input power, respectively. To test this method a 15 μm radius silicon microdisk and a 10 μm silicon nitride microdisk were characterized. During these tests it became clear that movement of the tapered fiber prohibited accurate determination of the non-linear absorption. An automated locking scheme was implemented to largely correct for these problems. The measurements of the non-linear absorption as a function of internal cavity energy U_c for the silicon and silicon nitride both roughly matched expectations based on literature values or intuition for the input powers that were tested. The accuracy of the non-linear absorption was mainly limited by the instability of the tapered fiber; using a fixed waveguide would probably provide a fix to this problem. Measurements of the linear absorption for the silicon microdisk did not match literature values or the value for the absorption as found with the radius-varying measurement of the same sample. The non-linear absorption as a function of U_c for the silicon nitride microdisk was a constant, which prohibited the determination of the linear absorption with the power-varying measurement method. Improvements for the power-varying measurement method can be sought in the improvement of the fitting of the measured doublet resonances, the better subtraction of background signals and the improved determination of the depth of the resonance dip and the resonance wavelength.

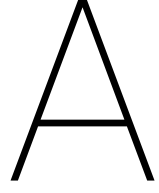
Stripped-oxide measurement method

The stripped-oxide measurement method was developed to determine the amount of material that is removed when performing an oxidizing fabrication process on silicon and afterwards stripping this oxide. This method was performed on silicon microdisks with a radius of 5 μm . The thickness of the stripped oxidized

material produced by a Piranha clean, an RCA-1 clean and an RCA-2 clean and a subsequent oxide strip were determined to be on average 1.4 ± 0.3 nm, 2.3 ± 0.5 nm and 0.75 ± 0.4 nm respectively. The qualitative comparison of the different fabrication processes correspond to the experiences of the other members of the research group.

Acknowledgements

My thanks go out all the people that have helped me during this research and the writing of my thesis. I would like to thank Dr. Simon Gröblacher for the opportunity to write my Master thesis as a part of his lab in the past year and to learn a lot by doing so. I would also like to thank my daily supervisor Andreas Wallucks for helping me during the experimental work, providing the samples and for the feedback given on my thesis. During my time as a part of the Gröblacher-lab I also received a lot of much appreciated advice from the other group members and my thanks go out to them. Last but not least I would like to thank the Delft University of Technology and all the support staff that have facilitated me in the production of this thesis.



Derivations

A.1. Derivation of the doublet Lorentzian transmission

As shown in section A.3, due to the backscattering of the light traveling in the microdisk due to the surface roughness of the disk coupling between the modes arises. By using a time-dependent perturbation theory it is possible to derive the coupled mode equations for the amplitude of the resonant modes. The differential equation for the amplitude a_k of mode k is given by [9]

$$\frac{da_k}{dt} + i\Delta\omega_k a_k(t) = i \sum_j \beta_{jk} a_j, \quad (\text{see A.25a})$$

where $\Delta\omega_k = \omega_k - \omega_0$ and β_{jk} is the scattering parameter between mode j and k . This formalism is applied to the microdisk system, where there are clockwise and counterclockwise modes. When all other modes are far off-resonance, the system of equations becomes

$$\frac{da_{cw}}{dt} = -i\Delta\omega a_{cw}(t) + i\frac{\gamma\beta}{2} a_{ccw}(t) \quad (\text{A.1a})$$

$$\frac{da_{ccw}}{dt} = -i\Delta\omega a_{ccw}(t) + i\frac{\gamma\beta}{2} a_{cw}(t), \quad (\text{A.1b})$$

where $\beta_{cw,ccw} = \beta_{ccw,cw} \equiv \gamma\beta/2$ and $\Delta\omega_{cw} = \Delta\omega_{ccw} \equiv \Delta\omega$. The next step is to add a coupling coefficient κ , which couples incoming light from a waveguide into the microdisk with an input power $|s|^2$ into the a_{cw} mode and a phenomenological loss rate γ_t which is split between the clockwise and counterclockwise modes [9]

$$\frac{da_{cw}}{dt} = -\left(\frac{\gamma_t}{2} + i\Delta\omega\right) a_{cw}(t) + i\frac{\gamma\beta}{2} a_{ccw}(t) + \kappa s \quad (\text{A.2a})$$

$$\frac{da_{ccw}}{dt} = -\left(\frac{\gamma_t}{2} + i\Delta\omega\right) a_{ccw}(t) + i\frac{\gamma\beta}{2} a_{cw}(t). \quad (\text{A.2b})$$

In these equations γ_t can be broken down in loss of light due to the coupling back into the waveguide, γ_{ext} , and all other loss, γ_i : $\gamma_t = \gamma_{\text{ext}} + \gamma_i$. It can also be shown that $\kappa^2 = \gamma_{\text{ext}}$ [9]. By changing the representation of the coupled mode formalism in the form of standing modes a_c and a_s instead of traveling waves using [16]

$$a_c = \frac{1}{\sqrt{2}}(a_{cw} + a_{ccw}), \text{ and } a_s = \frac{1}{\sqrt{2}}(a_{cw} - a_{ccw}) \quad (\text{A.3})$$

the differential equations have become uncoupled:

$$\frac{da_c}{dt} = \left(i\Delta\omega + i\frac{\gamma\beta}{2} - \frac{\gamma_c}{2}\right) a_c + \frac{\kappa}{\sqrt{2}} s \quad (\text{A.4a})$$

$$\frac{da_s}{dt} = \left(i\Delta\omega - i\frac{\gamma\beta}{2} - \frac{\gamma_s}{2}\right) a_s + \frac{\kappa}{\sqrt{2}} s \quad (\text{A.4b})$$

where γ_t has been replaced by the loss rates $\gamma_c = \gamma_{c,i} + \gamma_{\text{ext}}$ and $\gamma_s = \gamma_{s,i} + \gamma_{\text{ext}}$ to allow for different linewidths for the two standing modes. By using the expressions $T = |-s + \kappa a_{cw}|^2$ and $R = |\kappa a_{ccw}|^2$ for transmission and

reflection respectively [47] and inverting equation A.3, the following equations for steady-state transmission and reflection are obtained:

$$T = |-\sqrt{P_i} + \sqrt{\gamma_{\text{ext}}/2}(a_c + a_s)|^2 \quad (\text{A.5a})$$

$$R = |\sqrt{\gamma_{\text{ext}}/2}(a_c - a_s)|^2 \quad (\text{A.5b})$$

$$(\text{A.5c})$$

with

$$a_c = \frac{-\sqrt{\gamma_{\text{ext}}/2}\sqrt{P_i}}{-(\gamma_c/2) + i(\Delta\omega + \gamma_\beta/2)} \text{ and } a_s = \frac{-\sqrt{\gamma_{\text{ext}}/2}\sqrt{P_i}}{-(\gamma_s/2) + i(\Delta\omega - \gamma_\beta/2)}. \quad (\text{A.6})$$

A.2. Derivation of Q_{ss} equation

The derivation of the equation for the surface scattering Q factor, Q_{ss} , will be done based on the volume current method [20] and will follow the treatment as described in reference [9]. The scattering is a consequence of the polarization currents that originate from the index perturbations $\delta\epsilon$ on the edge of the disk. These perturbations are a consequence of damages due to the shape or composition of the edge of the material due to the fabrication process and the etching process in particular. It is assumed to be constant in the \hat{z} -direction and can therefore be approximated by [9]

$$\delta\epsilon(\vec{r}) = \epsilon_0 \delta n^2 h \Delta r(\phi) \delta(\rho - R) \delta(z), \quad (\text{A.7})$$

where $\delta n^2 = n_d^2 - n_0^2$, n_d and n_0 are the refractive indices of the microdisk and the environment, h and R are the thickness and the radius of the microdisk and $\Delta r(\phi)$ is the radial surface roughness relative to the unperturbed disk radius. These index perturbations create a polarization current which is approximated by a current that is sourced by the electric field solutions of the unperturbed disk \vec{E}^0

$$\vec{J} = -i\omega\delta\epsilon\vec{E}^0. \quad (\text{A.8})$$

This polarization current sources the vector potential that is given by [9]

$$\vec{A}_{\text{rad}}(\vec{r}) = \frac{\mu_0}{4\pi} \left(\frac{e^{-ik_1 r}}{r} \right) \int \vec{J}(\vec{r}') e^{-ik_1 \hat{r} \cdot \vec{r}'} d\vec{r}' \quad (\text{A.9})$$

where $k_1 \equiv k_0 n_0$, the wave number in the medium surrounding the microdisk. Now equations A.7 and A.8 are substituted into equation A.9 and $\vec{E}^0 = \vec{E}_m(\rho, z) e^{im\phi}$, where m is the azimuthal mode number, is taken as the electric field at the edge of the disk [9]

$$\vec{A}_{\text{rad}}(\vec{r}) = \frac{-i\mu_0\omega h \delta n^2 \epsilon_0 \vec{E}_m(R, 0) R}{4\pi} \left(\frac{e^{-ik_1 r}}{r} \right) \int_0^{2\pi} \Delta r(\phi') e^{im\phi'} e^{ik_1 R \sin(\theta) \cos(\phi')} d\phi'. \quad (\text{A.10})$$

This integral cannot yet be solved due to the fact that the function for the surface roughness $\Delta r(\phi)$ is random in nature. It can be solved statistically when the surface roughness becomes smaller than the wavelength of the light in the material. For light with a wavelength of 1550 nm in a silicon microdisk with $n_d = 3.48$, this becomes 445 nm. When this requirement is satisfied, it is assumed that any roughness along the arc length of the disk which is separated by more than a characteristic correlation length L_c is statistically independent. In this case each infinitesimal arc length along the edge of the disk, with its specific deviation from the perfect disk, can be treated as an ensemble member of all the possible outcomes under the same fabrication conditions. It is therefore possible to take an ensemble average over all these points [9]

$$\langle \vec{A}_{\text{rad}}(\vec{r}) \cdot \vec{A}_{\text{rad}}(\vec{r})^\dagger \rangle = \left| \frac{\mu_0\omega h \delta n^2 \epsilon_0 \vec{E}_m(R, 0)}{4\pi} \right|^2 \left(\frac{R}{r} \right)^2 \Theta, \quad (\text{A.11})$$

where the symbol \dagger indicates the complex conjugate, with

$$\Theta \equiv \int_0^{2\pi} \int_0^{2\pi} C(|\phi' - \phi''|) e^{im(|\phi' - \phi''|)} e^{ik_1 R \sin(\theta) [\cos(\phi') - \cos(\phi'')]} d\phi' d\phi'', \quad (\text{A.12})$$

where $C(|\phi' - \phi''|) = \langle \Delta r(\phi') \Delta(\phi'') \rangle$ is the correlation function for the disk roughness. By applying the approximations $t = \phi' - \phi''$ and $z = (\phi' + \phi'')/2$, the expression for Θ becomes [9]

$$\Theta = 2\pi \int_0^{2\pi} C(t) e^{imt} J_0 \left[2k_1 R \sin(\theta) \sin\left(\frac{t}{2}\right) \right] dt, \quad (\text{A.13})$$

with $J_0(x)$ a Bessel function of the first order. By applying a variable substitution, the integral can be written as an integral as a function of the arc length of the disk s over the interval $-\pi R$ to πR . For the correlation function a Gaussian model is assumed, which is given by $C(s) = \sigma_r^2 e^{-s^2/L_c^2}$. The resulting integral is given by [9]

$$\Theta = \frac{2\pi}{R} \int_{-\pi R}^{\pi R} \sigma_r^2 e^{-\frac{s^2}{L_c^2} + i\frac{m}{R}s} J_0 \left[2k_1 R \sin(\theta) \sin\left(\frac{sR}{2}\right) \right] ds. \quad (\text{A.14})$$

If the Gaussian function drops off quickly enough, i.e. $\pi R \gg L_c$, the domain of integration can be approximated as being infinite in positive and negative directions and the oscillating functions in the form of the imaginary exponential and the Bessel function can be neglected; the only thing that is left is a simple integration of a Gaussian over a infinite line, resulting in [9]

$$\Theta \simeq \frac{2\pi^{3/2} \sigma_r^2 L_c}{R}. \quad (\text{A.15})$$

When recombining equations A.11 and A.15, the far field Poynting vector can be given by [9, 20]

$$\langle \vec{S}_{\text{rad.}} \rangle = \hat{\mathbf{r}} \frac{\omega k_0}{2\mu_0} \langle |\vec{\mathbf{r}} \times \vec{\mathbf{A}}_{\text{rad.}}|^2 \rangle = \hat{\mathbf{r}} \frac{\omega k_1^3 n_0 (\delta n^2)^2 V_s^2 \epsilon_0 |\vec{\mathbf{E}}_m(R, 0)|^2}{16\sqrt{\pi}} \frac{|\hat{\mathbf{r}} \times \hat{\mathbf{e}}|^2}{r^2}, \quad (\text{A.16})$$

where $V_s \equiv \sqrt{RL_c} h \sigma_r$ is the effective volume of a typical scatterer. To calculate the total power radiated $P_{\text{rad.}}$, the Poynting vector is integrated over all angles

$$P_{\text{rad.}} = \iint (\vec{\mathbf{S}} \cdot \hat{\mathbf{r}}) r^2 \sin(\theta) d\theta d\phi = \sum_{\hat{\boldsymbol{\eta}}} \frac{\pi^{7/2} \omega n_0 (\delta n^2)^2 V_s^2 \epsilon_0 |E_m(R, 0; \hat{\boldsymbol{\eta}})|^2 G(\hat{\boldsymbol{\eta}})}{\lambda_0^3}, \quad (\text{A.17})$$

where $\hat{\boldsymbol{\eta}} = \{\hat{\boldsymbol{\rho}}, \hat{\boldsymbol{\phi}}, \hat{\boldsymbol{z}}\}$ and $G(\hat{\boldsymbol{\eta}}) = \{2/3, 2, 4/3\}$ is a geometrical radiation factor for the different electric field polarizations.

The surface scattering quality factor is given by [9]

$$Q_{\text{ss}} = \frac{\omega U_c}{P_{\text{rad.}}} = \frac{\lambda_0^3}{\pi^{7/2} n_0 (\delta n^2)^2 V_s^2 \sum_{\hat{\boldsymbol{\eta}}} \bar{u}_s(\hat{\boldsymbol{\eta}}) G(\hat{\boldsymbol{\eta}})} \quad (\text{A.18})$$

where $\bar{u}_s(\hat{\boldsymbol{\eta}})$ is the normalized, spatially-averaged $\hat{\boldsymbol{\eta}}$ -polarized electric field energy density at the disk edge given by

$$\bar{u}_s(\hat{\boldsymbol{\eta}}) = \frac{\epsilon_0 |\vec{\mathbf{E}}^0(\hat{\boldsymbol{\eta}})|_{\text{s,avg}}^2}{\frac{1}{2} \int \epsilon^0(\vec{\mathbf{r}}) |\vec{\mathbf{E}}^0|^2 d\vec{\mathbf{r}}}, \quad (\text{A.19})$$

and U_c is the internal cavity energy

$$U_c = \frac{1}{2} \int \epsilon^0(\vec{\mathbf{r}}) |\vec{\mathbf{E}}^0|^2 d\vec{\mathbf{r}}. \quad (\text{A.20})$$

Values for L_c and σ_r can be obtained by fitting equation A.30 for Q_β derived in section A.3 to the measured data. An expression for $\bar{u}_s(\hat{\boldsymbol{\eta}})$ is derived in section 2.3.3.

A.3. Derivation of Q_β equation

In a perfect disk the clockwise (cw) and counterclockwise (ccw) traveling waves will be degenerate. Due to the surface roughness of the microdisk these modes will be coupled and the degeneracy will be lifted; two standing wave modes with a down- and upshifted frequency will form. This splitting, γ_β , can be quantified with a time-dependent perturbation theory and subsequently be linked to the correlation length L_c and the amplitude σ_r of the surface roughness. This derivation follows the work published in reference [9].

Just as in section A.2, the surface roughness is treated as an index perturbation $\delta\epsilon$, shown in equation A.7, which produces a polarization current $\vec{J}(\vec{r})$, as shown in equation A.8. If this polarization current is added as a source to the Maxwell equations and from these a wave function is derived, this will be [9]

$$\nabla^2 \vec{E} - \mu_0(\epsilon^0(\vec{r}) + \delta\epsilon(\vec{r})) \frac{\partial^2 \vec{E}}{\partial t^2} = 0. \quad (\text{A.21})$$

where $\epsilon^0(\vec{r})$ is the dielectric structure for the ideal disk. The modes that form a solution of the unperturbed wave function are taken as $\vec{E}_j^0(\vec{r}, t) = \vec{E}_j^0(\vec{r})e^{-i\omega_j t}$, where the index j corresponds to all possible types of oscillations and $j = 0$ corresponds to the initially excited mode. These modes satisfy the wave equation

$$\nabla^2 \vec{E}_j^0(\vec{r}) + \mu_0\epsilon^0(\vec{r})\omega_j^2 \vec{E}_j^0(\vec{r}) = 0. \quad (\text{A.22})$$

The assumption is that the solution of the perturbed wave equation is given by a linear combination of the unperturbed modes weighed with slowly varying coefficients $a_j(t)$ [9]

$$\vec{E}(\vec{r}) = e^{-i\omega_0 t} \sum_j a_j(t) \vec{E}_j^0(\vec{r}). \quad (\text{A.23})$$

By entering this solution into equation A.21, using equation A.22 and keeping only first order terms, the following equation is derived [9]

$$\sum_j \left(2i\omega_0\epsilon^0 \frac{da_j}{dt} + \delta\epsilon\omega_0^2 a_j - \epsilon^0(\omega_j^2 - \omega_0^2) a_j \right) \vec{E}_j^0(\vec{r}) = 0. \quad (\text{A.24})$$

By multiplying the equation with $(\vec{E}_j^0(\vec{r}))^\dagger$ and integrating over the whole space, the relation $\int \epsilon^0(\vec{r}) (\vec{E}_j^0(\vec{r}))^\dagger \vec{E}_k^0(\vec{r}) d\vec{r} = 0$ for $j \neq k$ can be used to obtain [9]

$$\frac{da_k}{dt} + i\Delta\omega_k a_k(t) = i \sum_j \beta_{jk} a_j, \quad (\text{A.25a})$$

$$\text{with } \beta_{jk} = \frac{\omega_0}{2} \frac{\int \delta\epsilon(\vec{r}) (\vec{E}_j^0(\vec{r}))^\dagger \vec{E}_k^0(\vec{r}) d\vec{r}}{\int \epsilon^0(\vec{r}) |\vec{E}_k^0(\vec{r})|^2 d\vec{r}} \quad (\text{A.25b})$$

where $\Delta\omega_k = \omega_k - \omega_0$. The radius of the ideal disk in $\epsilon^0(\vec{r})$ is chosen as the average radius of the perturbed disk to make sure that the strength of the perturbation does not create a self-term frequency shift, i.e. $\beta_{jj} = 0$.

The next step is to apply this coupled mode formalism to the case of a microdisk system in which there initially are degenerate clockwise and counterclockwise modes, which is resonantly pumped with an external waveguide. For small perturbations, the assumption can be made that the backscattering rate for each mode is identical, so $\beta_{\text{cw},\text{ccw}} = \beta_{\text{ccw},\text{cw}} \equiv \gamma_\beta/2$. When all other modes are far off-resonance, they can be neglected. To derive an expression for $\gamma_\beta/2$, equations A.7 and A.20 are substituted into equation A.25b, resulting in [9]

$$\frac{\gamma_\beta}{2} = \frac{\omega_0}{4U_c} \int \epsilon_0 \delta n^2 h \Delta r(\phi) \delta(r - R) \delta(z) (\vec{E}_{\text{cw}}(\vec{r}))^\dagger \vec{E}_{\text{ccw}}(\vec{r}) d\vec{r}. \quad (\text{A.26})$$

At the disk edge in the $\rho - \phi$ plane, the electric fields can be expressed as $\vec{E}_{\text{cw}} = \vec{E}_m(R, 0)e^{-im\phi}$ and $\vec{E}_{\text{ccw}} = \vec{E}_m(R, 0)e^{im\phi}$. Evaluating the integral will therefore give the expression [9]

$$\frac{\gamma_\beta}{2} = \frac{\omega_0 \delta n^2 h R \epsilon_0 |\vec{E}_m(R, 0)|^2}{4U_c} Y \quad (\text{A.27a})$$

$$\text{with } Y = \int_0^{2\pi} \Delta r(\phi) e^{i2m\phi} d\phi. \quad (\text{A.27b})$$

Similar as in section A.2, the integral for Y can be solved statistically when the surface roughness becomes smaller than the wavelength in the material. The ensemble average is calculated in the same way and with the same approximations as in section A.2, resulting in [9]

$$\langle Y \cdot Y^\dagger \rangle \approx \frac{2\pi}{R} \int_{-R}^R \sigma_r^2 e^{-\frac{s^2}{l_c^2} + i\frac{m}{R}s} ds \approx \frac{2\pi^{3/2} \sigma_R^2 L_c}{R}. \quad (\text{A.28})$$

Substituting equation A.28 into equation A.26 [9]

$$\sqrt{\left\langle \left(\frac{\gamma_\beta}{2} \right)^2 \right\rangle} \approx \frac{\sqrt{RL_c} \sigma_r h \omega_0 \delta n^2 (\pi/4)^{3/4} \epsilon_0 |\vec{E}_m(R, 0)|^2}{U_c} \approx V_s \omega_0 \delta n^2 \frac{\pi^{3/4}}{4} \sum_{\hat{\eta}} \bar{u}_s(\hat{\eta}). \quad (\text{A.29})$$

As specified in equation 2.8, the quantity Q_β is defined as [9]

$$Q_\beta \equiv \frac{\omega_0}{\gamma_\beta} \approx \frac{\sqrt{2}}{\pi^{3/4} \delta n^2 V_s \sum_{\hat{\eta}} \bar{u}_s(\hat{\eta})}. \quad (\text{A.30})$$

By fitting equation A.30 to the measurements of Q_β of microdisks with different radii, the value for $\sqrt{L_c} \sigma_r$ can be determined. With this, parameter Q_{ss} can be calculated with equation A.18.

Bibliography

- [1] M. Aspelmeyer, T. J. Kippenberg, and F. Marquardt. Cavity optomechanics. *Reviews of Modern Physics*, 86(4):1391, 2014.
- [2] B. P. Abbott, R. Abbott, R. Adhikari, P. Ajith, B. Allen, G. Allen, R. S. Amin, S. B. Anderson, W. G. Anderson, M. A. Arain, et al. Ligo: the laser interferometer gravitational-wave observatory. *Reports on Progress in Physics*, 72(7):076901, 2009.
- [3] J. Chan, T. P. Mayer Alegre, A. H. Safavi-Naeini, J. T. Hill, A. Krause, S. Gröblacher, M. Aspelmeyer, and O. Painter. Laser cooling of a nanomechanical oscillator into its quantum ground state. *Nature*, 478(7367):89, 2011.
- [4] S. Hong, R. Riedinger, I. Marinkovic, A. Wallucks, S. G. Hofer, R. A. Norte, M. Aspelmeyer, and S. Gröblacher. Hanbury brown and twiss interferometry of single phonons from an optomechanical resonator. *Science*, 358(6360):203–206, 2017.
- [5] R. Riedinger, S. Hong, R. A. Norte, J. A. Slater, J. Shang, A. G. Krause, V. Anant, M. Aspelmeyer, and S. Gröblacher. Non-classical correlations between single photons and phonons from a mechanical oscillator. *Nature*, 530(7590):313–316, 2016.
- [6] R. A. Norte, J. P. Moura, and S. Gröblacher. Mechanical resonators for quantum optomechanics experiments at room temperature. *Physical review letters*, 116(14):147202, 2016.
- [7] S. A. Miller, M. Yu, X. Ji, A. G. Griffith, J. Cardenas, A. L. Gaeta, and M. Lipson. Low-loss silicon platform for broadband mid-infrared photonics. *arXiv preprint arXiv:1703.03517*, 2017.
- [8] A. I. Kuznetsov, A. E. Miroschnichenko, M. L. Brongersma, Y. S. Kivshar, and B. Luk'yanchuk. Optically resonant dielectric nanostructures. *Science*, 354(6314):aag2472, 2016.
- [9] M. Borselli, T. J. Johnson, and O. Painter. Beyond the rayleigh scattering limit in high-q silicon microdisks: theory and experiment. *Optics Express*, 13(5):1515–1530, 2005.
- [10] M. Borselli, T. J. Johnson, and O. Painter. Accurate measurement of scattering and absorption loss in microphotonic devices. *Optics letters*, 32(20):2954–2956, 2007.
- [11] F. W. Kern. Cleaning solutions based on hydrogen peroxide for use in silicon semiconductor technology. *RCA Rev.*, 31:187, 1970.
- [12] C. P. Michael. *Optical material characterization using microdisk cavities*. PhD thesis, California Institute of Technology, 2009.
- [13] K. J. Vahala. Optical microcavities. *nature*, 424(6950):839, 2003.
- [14] J. C. Knight, G. Cheung, F. Jacques, and T. A. Birks. Phase-matched excitation of whispering-gallery-mode resonances by a fiber taper. *Optics letters*, 22(15):1129–1131, 1997.
- [15] Lord Rayleigh. Cxii. the problem of the whispering gallery. *The London, Edinburgh, and Dublin Philosophical Magazine and Journal of Science*, 20(120):1001–1004, 1910.
- [16] M. Borselli. *High-Q microresonators as lasing elements for silicon photonics*. PhD thesis, California Institute of Technology, 2006.
- [17] COMSOL AB. Comsol multiphysics® v. 5.0. Stockholm, Sweden, 2014, www.comsol.com.
- [18] T. Johnson. *Silicon microdisk resonators for nonlinear optics and dynamics*. California Institute of Technology, 2009.

- [19] P. E. Barclay, K. Srinivasan, and O. Painter. Nonlinear response of silicon photonic crystal microresonators excited via an integrated waveguide and fiber taper. *Optics express*, 13(3):801–820, 2005.
- [20] M. Kuznetsov and H. Haus. Radiation loss in dielectric waveguide structures by the volume current method. *IEEE journal of quantum electronics*, 19(10):1505–1514, 1983.
- [21] B. E. Little and S. T. Chu. Estimating surface-roughness loss and output coupling in microdisk resonators. *Optics letters*, 21(17):1390–1392, 1996.
- [22] C. P. Dettmann, G. V. Morozov, M. Sieber, and H. Waalkens. Tm and te directional modes of an optical microdisk resonator with a point scatterer. In *Transparent Optical Networks, 2008. ICTON 2008. 10th Anniversary International Conference on*, volume 4, pages 65–68. IEEE, 2008.
- [23] A. Yariv. *Optical electronics*. Saunders College Publ., 1991.
- [24] M. Abramowitz and I. A. Stegun. *Handbook of mathematical functions: with formulas, graphs, and mathematical tables*, volume 55. Courier Corporation, 1964.
- [25] Wolfram Research, Inc. Mathematica, Version 11.2. Champaign, IL, 2017.
- [26] *Santec TSL-510 Operation Manual*. Santec Corporation, 2005.
- [27] R. Paschotta. Article on 'external-cavity diode lasers' in the encyclopedia of laser physics and technology. https://www.rp-photonics.com/external_cavity_diode_lasers.html. Accessed on 27-6-2017.
- [28] *Sercalo VP1-9N-12-16 Manual*. Sercalo Microtechnology Ltd.
- [29] K. Srinivasan, P. E. Barclay, M. Borselli, and O. Painter. Optical-fiber-based measurement of an ultrasmall volume high-q photonic crystal microcavity. *Physical Review B*, 70(8):081306, 2004.
- [30] B. S. Kawasaki, K. O. Hill, and R. G. Lamont. Biconical-taper single-mode fiber coupler. *Optics Letters*, 6(7):327–328, 1981.
- [31] B. D. Hauer, P. H. Kim, C. Doolin, A. J. R. MacDonald, H. Ramp, and J. P. Davis. On-chip cavity optomechanical coupling. *EPJ Techniques and Instrumentation*, 1(1):4, 2014.
- [32] T. A. Birks and Y. W. Li. The shape of fiber tapers. *Journal of Lightwave Technology*, 10(4):432–438, 1992.
- [33] M. Cai and K. Vahala. Highly efficient optical power transfer to whispering-gallery modes by use of a symmetrical dual-coupling configuration. *Optics Letters*, 25(4):260–262, 2000.
- [34] D. K. Armani, T. J. Kippenberg, S. M. Spillane, and K. J. Vahala. Ultra-high-q toroid microcavity on a chip. *Nature*, 421(6926):925, 2003.
- [35] H. H. Ku. Notes on the use of propagation of error formulas. *Journal of Research of the National Bureau of Standards*, 70(4), 1966.
- [36] P. T. Boggs and J. E. Rogers. Orthogonal distance regression. *Contemporary Mathematics*, 112:183–194, 1990.
- [37] A. M. Jones, A. L. Lentine, C. T. DeRose, A. L. Starbuck, A. Pomerene, and R. A. Norwood. Efficient coefficient extraction from doublet resonances in microphotonic resonator transmission functions. In *Lasers and Electro-Optics (CLEO), 2015 Conference on*, pages 1–2. IEEE, 2015.
- [38] G. Cocorullo and I. Rendina. Thermo-optical modulation at 1.5 μm in silicon etalon. *Electronics Letters*, 28(1):83–85, 1992.
- [39] A. Arbabi and L. L. Goddard. Measurements of the refractive indices and thermo-optic coefficients of Si_3N_4 and SiO_x using microring resonances. *Optics letters*, 38(19):3878–3881, 2013.
- [40] H. H. Li. Refractive index of silicon and germanium and its wavelength and temperature derivatives. *Journal of Physical and Chemical Reference Data*, 9(3):561–658, 1980.

- [41] K. Luke, Y. Okawachi, M. R. E. Lamont, A.L. Gaeta, and M. Lipson. Broadband mid-infrared frequency comb generation in a Si_3N_4 microresonator. *Optics letters*, 40(21):4823–4826, 2015.
- [42] M. G. Burzo, P. .L Komarov, and P. E. Raad. Non-contact thermal conductivity measurements of p-doped and n-doped gold covered natural and isotopically-pure silicon and their oxides. In *Thermal and Mechanical Simulation and Experiments in Microelectronics and Microsystems, 2004. EuroSimE 2004. Proceedings of the 5th International Conference on*, pages 269–276. IEEE, 2004.
- [43] M. Morita, T. Ohmi, E. Hasegawa, M. Kawakami, and M. Ohwada. Growth of native oxide on a silicon surface. *Journal of Applied Physics*, 68(3):1272–1281, 1990.
- [44] D. K. Sparacin, S. J. Spector, and L. C. Kimerling. Silicon waveguide sidewall smoothing by wet chemical oxidation. *Journal of lightwave technology*, 23(8):2455, 2005.
- [45] H. Sun, A. Chen, D. Abeysinghe, A. Szep, and R. S. Kim. Reduction of scattering loss of silicon slot waveguides by rca smoothing. *Optics letters*, 37(1):13–15, 2012.
- [46] G. K. Celler, D. L. Barr, and J. M. Rosamilia. Etching of silicon by the rca standard clean 1. *Electrochemical and Solid-State Letters*, 3(1):47–49, 2000.
- [47] T. J. Kippenberg, S. M. Spillane, and K. J. Vahala. Modal coupling in traveling-wave resonators. *Optics letters*, 27(19):1669–1671, 2002.